ATLAS CONF Note

ATLAS-CONF-2020-001

13th February 2020

Measurements of top-quark pair single- and double-differential cross-sections in the all-hadronic channel in pp collisions at $\sqrt{s} = 13$ TeV using the ATLAS detector

The ATLAS Collaboration

Differential cross-sections are measured for top-quark pair production in the all-hadronic decay mode, using proton–proton collision events collected by the ATLAS experiment in which all six decay jets are separately resolved. Absolute and normalised single- and double-differential cross-sections are measured at particle and parton level as a function of various kinematic variables. Emphasis is placed on well-measured observables in fully-reconstructed final states, as well as on the study of correlations between the top-quark pair system and additional jet radiation identified in the event. The study is performed using data from proton–proton collisions at $\sqrt{s} = 13$ TeV collected by the ATLAS detector at CERN's Large Hadron collider in 2015 and 2016, corresponding to an integrated luminosity of 36.1 fb^{-1}. The rapidities of the individual top quarks and of the top-quark pair are well modelled. Significant mismodelling is observed in the transverse momenta of the leading three jet emissions, while the leading top-quark transverse momentum and top-quark pair transverse momentum are both found to be incompatible with several theoretical predictions.

ATLAS-CONF-2020-001
13 February 2020

1 Introduction

As the heaviest particle of the Standard Model (SM), the top quark and its properties provide insights on a wide range of topics, including proton structure and precision electroweak physics. Top-quark pair production is the most significant background to the bulk of searches for physics beyond the Standard Model (BSM); therefore, improving the accuracy of theoretical models for these production processes is of central importance to the collider physics programme.

The Large Hadron Collider [1] (LHC) is the first top-quark factory, and thus provides an unprecedented opportunity to study the physics of the top quark. This paper reports the results of measurements of differential cross-sections for the production of top-quark pairs in the final state with the largest branching ratio, namely the simultaneous decay of the two top quarks each to a bottom quark and two additional quarks. The measurements are performed in the six-jet topology, using data collected by the ATLAS detector [2] at a centre-of-mass energy ($\sqrt{s}$) of 13 TeV in 2015 and 2016 and corresponding to 36 fb^{-1} of proton–proton (pp) collisions.

Single- and double-differential distributions of the kinematic properties of the top-quark-antiquark ($t\bar{t}$) system are presented. They can be used to improve constraints on parton distribution functions (PDFs) and tuning of precision cross-section computations. Correlations between the $t\bar{t}$ system and associated jet production are also measured, to give information on predictions of multileg matrix-element calculations. Both absolute and normalised differential cross-sections are presented.

Previous differential measurements of top-quark cross sections, particularly in association with additional jets, have mainly used the lepton-plus-jets (ℓ+jets) and dileptonic decay modes [3–14], while the all-hadronic decay mode has been studied at lower $\sqrt{s}$ by the CMS collaboration [15, 16] and in the highly boosted regime, at high transverse momentum (p_{T}) [17], by the ATLAS collaboration. In this analysis, events are considered in which all three quarks from each top-quark decay are resolved into distinct jets, leading to at least six jets in the final state. This complements the measurements made in this channel using large-radius jets [17], which are limited to the region of top-quark transverse momentum above 350 GeV. The resolved all-hadronic final state is admittedly subject to a larger background contamination from multi-jet production. However, this final state avoids kinematic ambiguities due to the presence of neutrinos accompanying the leptonic decays. This allows a full reconstruction of the top-quark pair without recourse to the missing transverse momentum, which has a relatively poor experimental resolution and provides no information on longitudinal momentum. The good momentum resolution on both top quarks enables characterisation of the kinematic properties of additional jet radiation accompanying the $t\bar{t}$ system in relation to the top-quark pair kinematics.

Differential distributions measured in data are presented with corrections both to the stable particle level in a fiducial phase space, and to the parton level in the full phase space. The paper presents a set of measurements of the $t\bar{t}$ production cross section as a function of properties of the reconstructed top quark (transverse momentum and rapidity) and of the $t\bar{t}$ system (transverse momentum, rapidity and invariant mass) as well as additional variables. Taking various reference objects such as the leading top quark, the leading jet and the leading extra jet, angular separations and transverse momentum ratios between the additional jet radiation and these reference objects are measured. The measured differential cross-sections are compared with predictions from a variety of Monte Carlo (MC) event generators at next-to-leading-order (NLO): Powheg-Box v2 [18–21] and MadGraph5_aMC@NLO [22] interfaced with Pythia8 [23] and Herwig7 [24], and Sherpa v2.2 [25].

2 ATLAS detector

The ATLAS detector [2] is a multi-purpose particle physics detector with a forward–backward symmetric cylindrical geometry and nearly 4π coverage in solid angle, up to $|\eta| = 4.9$[1]. The layout of the detector is based on four superconducting magnet systems, which comprise a thin solenoid surrounding the inner tracking detectors (ID) and a barrel and two end-cap toroids generating the magnetic field for a large muon spectrometer. The ID is comprised of two silicon sub-detectors, namely an inner pixel detector and an outer strip tracker, inside a Transition Radiation Tracker (TRT) based on gas-filled drift tubes. The calorimeters are located between the ID and the muon system. The lead/liquid-argon (LAr) electromagnetic (EM) calorimeter is split into two regions: the barrel ($|\eta| < 1.475$) and the end-cap ($1.375 < |\eta| < 3.2$). The hadronic calorimeter is divided into four regions: the barrel ($|\eta| < 1.0$) and the extended barrel ($0.8 < |\eta| < 1.7$) made of scintillator/steel, the end-cap ($1.5 < |\eta| < 3.2$) with LAr/copper modules, and the forward calorimeter ($3.1 < |\eta| < 4.9$) composed of LAr/copper and LAr/tungsten modules.

A two-level trigger system [26] is used to select events for further analysis. The first level (L1) of the trigger reduces the event rate to about 100 kHz using hardware-based trigger algorithms acting on a subset of detector information. The second High-Level Trigger (HLT) uses a combination of fast online algorithms and reconstruction software with algorithms similar to the offline versions. The software-based trigger further reduces the average event rate to about 1000 Hz.

3 Collision data and simulated event samples

The data used for this analysis were recorded with the ATLAS detector from pp collisions at $\sqrt{s} = 13$ TeV in 2015 and 2016 with an average number of pp interactions per bunch crossing $\langle\mu\rangle$ of around 23. The selected data sample corresponds to an integrated luminosity of 36.1 fb^{-1} with an uncertainty of 2.1% [27] obtained using the LUCID-2 detector [28] for the primary luminosity measurements. Only the data collected while all sub-detectors were operational are considered.

The events for this analysis were collected using a multi-jet trigger. This trigger selects events containing six jets with a minimum p_{T} of 45 GeV in the central region of the detector; the η acceptance of all six jets changed from $|\eta| < 3.2$ in 2015 to $|\eta| < 2.4$ in 2016 to reduce triggered event rates. Jets at the HLT are reconstructed with the anti-k_t jet algorithm [29] using a radius parameter, R, of 0.4 and are calibrated. This trigger was chosen as it provides a high efficiency for signal events, but places no constraint on b-tagged jets, which is crucial for evaluating background contributions in data.

The physics processes of interest to this analysis are: $t\bar{t}$ events with both W-bosons decaying hadronically (all-hadronic signal), $t\bar{t}$ events with at least one W-boson decaying leptonically (non-all-hadronic background) and multi-jet production from purely strong interaction processes (multi-jet background).

[1] ATLAS uses a right-handed Cartesian coordinate system with its origin at the nominal interaction point (IP) in the centre of the detector. The z-axis is taken along the beam pipe, and the x-axis points from the IP to the centre of the LHC ring. Cylindrical coordinates (r, ϕ) are used in the transverse plane, ϕ being the azimuthal angle around the beam pipe. The rapidity y is defined by $\frac{1}{2} \ln \frac{E+p_z}{E-p_z}$, while the pseudorapidity is defined in terms of the polar angle θ as $\eta = -\ln \tan(\theta/2)$.

3.1 Top pair simulation samples

Tthe MC generators listed in Table 1 are used to simulate $t\bar{t}$ event samples for unfolding corrections (Section 8), systematic uncertainty estimates and comparison with results at the pre- and post-unfolding level. The top-quark mass (m_t) and width were set to 172.5 GeV and 1.32 GeV, respectively, in all MC event generators.

Application	$t\bar{t}$ signal	$t\bar{t}$ radiation syst.		$t\bar{t}$ PS syst.	$t\bar{t}$ ME syst.	$t\bar{t}$ comparison
Generator	Powheg-Box v2				MadGraph5/ aMC@NLO 2.6.0	Sherpa 2.2.1
σ precision	NNLO + NNLL					
PDF for ME	NNPDF3.0NLO					
Parton shower	Pythia8			Herwig7	Pythia8	ME+PS@NLO
PDF for PS	NNPDF2.3LO			MMHT2014	NNPDF2.3LO	
Tune	A14	Var3cUp	Var3cDown	H7UEMMHT	A14	–
Scales	$h_{\text{damp}} = 1.5 m_t$	$h_{\text{damp}} = 3 m_t$ $\mu_{\text{R,F}} = 0.5$	$h_{\text{damp}} = 1.5 m_t$ $\mu_{\text{R,F}} = 2.0$	$h_{\text{damp}} = 1.5 m_t$	$\mu_q = H_{\text{T}}/2$	–

Table 1: Summary of $t\bar{t}$ MC samples used in the analysis, showing the generator for the hard-scattering process, cross-section (σ) normalisation precision, PDF choices for the hard process matrix element (ME) and parton shower (PS), as well as the parton shower and hadronisation generator and the corresponding tune and scales.

The EvtGen v1.2.0 program [30] was used to simulate the decay of bottom and charm hadrons, except for samples generated with Sherpa [25]. Multiple overlaid pp collisions (pile-up) were simulated with the low-p_{T} QCD processes of Pythia 8.186 [23] using a set of tuned parameters called the A3 tune [31] and the NNPDF2.3LO [32] set of parton distribution functions (PDFs).

The detector response is simulated using the Geant4 framework [33, 34]. The data and MC events were reconstructed with the same software algorithms.

For the generation of $t\bar{t}$ events, matrix elements (ME) were calculated at NLO in QCD using the Powheg-Box v2 [19, 20] event generator with the NNPDF3.0NLO PDF set [35]. Pythia 8.210 with the NNPDF2.3LO [36] PDF set and the A14 [37] tune was used to simulate the parton shower, fragmentation and underlying event. The h_{damp} parameter, which controls the p_{T} of the first gluon or quark emission beyond the Born configuration in Powheg-Box v2, was set to 1.5 m_t. The main effect of this parameter is to regulate the high-p_{T} emission against which the $t\bar{t}$ system recoils. A dynamic value $\sqrt{m_t^2 + p_{\text{T},t}^2}$ was used for the factorisation and renormalisation scales (μ_{F} and μ_{R} respectively). Signal $t\bar{t}$ events generated with those settings are referred to as the nominal signal sample.

The effects of different levels of initial state radiation (ISR) were evaluated using two samples with different factorisation and renormalisation scales relative to the nominal signal sample, as well as a different h_{damp} parameter value. Specifically, two settings for Powheg+Pythia8 were compared [38]:

- in one sample $\mu_{\text{F,R}}$ were reduced by a factor of 0.5, the h_{damp} parameter is increased to 3 m_t and the Var3cUp A14 tune variation was used. In all the following Figures and Tables the predictions based on this MC sample are referred to as 'PWG+PY8 Up';
- in the other sample $\mu_{\text{F,R}}$ were increased by a factor of 2, the h_{damp} parameter was set to 1.5 m_t as in the nominal sample and the Var3cDown A14 tune variation was used. In all the following Figures and Tables the predictions based on this MC sample are referred to as 'PWG+PY8 Down'.

To estimate the effect of the parton shower and hadronisation algorithms, a POWHEG+HERWIG7 sample was generated with POWHEG set up in the same way as for the nominal sample. The parton shower, hadronisation and underlying event simulation were produced with HERWIG7 [24, 39] (version 7.0.4) using the MMHT2014LO68CL PDF set and H7-UE-MMHT tune [40]. Detector simulation was performed using a fast simulation based on a parameterisation of the performance of the ATLAS electromagnetic and hadronic calorimeters [41] (ATLFASTII) and on GEANT4 elsewhere.

The impact of the matrix element generator choice was evaluated using events generated with MADGRAPH5_aMC@NLO+PYTHIA8 at NLO accuracy. The events were generated with version 2.6.0 of MADGRAPH5_aMC@NLO [22] and $\mu_q = H_T/2$ for the shower starting scale functional form [42]. As for the POWHEG+PYTHIA8 samples, the NNPDF3.0NLO PDF set was used for the matrix element and the NNPDF2.3LO set for the parton shower. Calorimeter simulation was performed using ATLFASTII.

An additional sample of $t\bar{t}$ events generated with SHERPA 2.2.1 to provide an extra point of comparison [25]. This sample is produced at NLO in QCD for up to 1 additional parton emission, and LO for up to 4 additional partons, using the MEPSNLO merging scheme [43], with the CKKW merging scale fixed at 30 GeV [42]. Loop integrals were calculated with OpenLoops [44]. The shower, factorisation and renormalisation scales were set to $\mu = \sqrt{m_t^2 + 0.5(p_{\mathrm{T},t}^2 + p_{\mathrm{T},\bar{t}}^2)}$, and the NNPDF2.3LO PDF set was used.

The cross section used to normalise the $t\bar{t}$ samples was $\sigma_{t\bar{t}} = 832^{+20}_{-29}(\mathrm{scale}) \pm 35\ (\mathrm{PDF}, \alpha_S)$ pb, as calculated with the Top++2.0 program at NNLO in perturbative QCD, including soft-gluon resummation to next-to-next-to-leading-log order (NNLL) [21, 45–50], and assuming $m_t = 172.5$ GeV. The first uncertainty comes from the independent variation of the factorisation and renormalisation scales, μ_F and μ_R, while the second one is associated with variations in the PDF and α_S, following the PDF4LHC prescription with the MSTW2008 68% CL NNLO, CT10 NNLO and NNPDF2.3 5f FFN PDF sets, described in Refs. [36, 51–53].

Top-quark pair events in which at least one of the W-bosons decays via a lepton and a neutrino are a source of background contamination if the leptons are not identified. Simulated $t\bar{t}$ events with one or two leptonic decays are produced with the same settings used for the nominal signal sample.

4 Object reconstruction

The following sections describe the detector-, particle- and parton-level objects used to characterise the final-state event topology and to define the fiducial and full phase-space regions for the measurements. The final state of interest to this measurement includes jets, some of which may be b-tagged, but contains no isolated electrons, muons or tau leptons.

4.1 Detector-level object reconstruction

Primary vertices are formed from reconstructed tracks which are spatially compatible with the interaction region. The hard-scatter primary vertex is chosen to be the one with at least two associated tracks and the highest $\sum p_{\mathrm{T}}^2$, where the sum extends over all tracks with $p_{\mathrm{T}} > 0.4$ GeV matched to the vertex.

Jets are reconstructed from topological clusters of calorimeter cells that are noise-suppressed and calibrated to the electromagnetic scale [54] using the anti-k_t algorithm with a radius parameter $R = 0.4$ as implemented

in FastJet [55]. The jets are corrected using a subtraction procedure that accounts for the jet area to estimate and remove the average energy contributed by pile-up interactions [56]; these corrections can change the jet four-momentum. This procedure is followed by a jet-energy-scale (JES) calibration that restores the jet energy to the mean response of a particle-level simulation, refined by applying a series of additional calibrations that correct finer variations due to jet flavour and detector geometry and *in situ* corrections that match the data to the simulation energy scale [57].

Jets must satisfy $p_{\mathrm{T}} > 25$ GeV and $|\eta| < 2.5$ and pass the overlap removal with leptons, as described below. To reduce the number of jets that originate from pile-up, an additional requirement on the association of a jet to a vertex, the Jet Vertex Tagger (JVT) [58], is applied. Every jet in the range $p_{\mathrm{T}} < 60$ GeV and $|\eta| < 2.4$ must satisfy the criterion JVT > 0.59. The JVT discriminant is based on the degree of association to the hard scatter vertex of tracks matched to the jet through a ghost-association technique described in Ref. [59].

Jets containing b-hadrons are tagged as b-jets using a multivariate discriminant (MV2c10) [60]. It combines information from the impact parameters of displaced tracks and from the location and topological properties of secondary and tertiary decay vertices reconstructed within the jet. The jets are considered b-tagged if the value of the discriminant is larger than a threshold applied on the discriminant output value, chosen to provide a specific b-jet efficiency on an inclusive $t\bar{t}$ sample. In this analysis, a threshold corresponding to 70% b-jet efficiency is chosen. The corresponding rejection factors for jets initiated by charm quarks or lighter quark flavours are approximately 12 and 380, respectively [61].

Electron candidates are reconstructed from clusters of energy in the calorimeter combined with an inner detector (ID) track that is refitted using Gaussian Sum Filters and calibrated using a multivariate regression [62, 63]. They must satisfy $p_{\mathrm{T}} > 15$ GeV and $|\eta_{\mathrm{clus}}| < 1.37$ or $1.52 < |\eta_{\mathrm{clus}}| < 2.47$ and pass the "Tight" likelihood-based identification criterion based on shower shapes in the EM calorimeter, track quality and detection of transition radiation produced in the TRT detector [64]. Isolation requirements based on calorimeter and tracking quantities are used to reduce the background from jets misidentified as prompt leptons (fake leptons) or due to semi-leptonic decays of heavy-flavour hadrons (non-prompt real leptons) [63]. The isolation criteria are p_{T}- and η-dependent, and ensure an efficiency of 90% for electrons with p_{T} of 25 GeV and 99% efficiency for electrons with p_{T} of 60 GeV.

Muon candidates are reconstructed using high-quality ID tracks combined with tracks reconstructed in the muon spectrometer [65]. They must satisfy $p_{\mathrm{T}} > 15$ GeV, $|\eta| < 2.5$. To reduce the background from muons originating from heavy-flavour decays inside jets, muons are required to be isolated using track quality and isolation criteria similar to those applied to electrons.

Hadronically decaying τ-lepton (τ_{had}) candidates are reconstructed from hadronic jets associated with either one or three ID tracks with a total charge of ± 1 [66, 67]. Tau candidates with $p_{\mathrm{T}} > 25$ GeV and $|\eta| < 2.5$ are considered. A Boosted Decision Tree (BDT) discriminant is used to distinguish τ_{had} candidates from quark- or gluon-initiated jets, for which the "Medium" working point is used. A second BDT is used to eliminate electrons faking a τ, for which a "Loose" working point was selected.

For objects satisfying both the jet and lepton selection criteria, a procedure called "overlap removal" is applied to assign objects a unique particle hypothesis, favouring well identified and isolated particles. If an electron candidate shares a track with a muon candidate, the electron is removed, as it is likely to result from final state radiation (FSR). If a jet and an electron are within $\Delta R = \sqrt{\Delta\eta^2 + \Delta\phi^2} < 0.2$ the jet is discarded. If the distance in ΔR between a surviving jet and an electron is smaller than 0.4, then the electron is discarded. If a muon track is ghost-associated to a jet, or a jet and a muon are within $\Delta R < 0.2$, then the jet is removed if its p_{T}, total track p_{T} and number of tracks are consistent with muon FSR or

energy loss. If the distance in ΔR between a jet and a muon candidate is $\Delta R < 0.4$, the muon is discarded; otherwise the jet is removed. Finally, if the distance in ΔR between a jet and a tau jet is $\Delta R < 0.2$, then the jet is discarded.

4.2 Particle- and parton-level objects and phase-spaces definition

Particle-level objects are defined in simulated events using only stable particles, i.e. particles with a mean lifetime $\tau > 30$ ps. The fiducial phase space for the measurements presented in this paper is defined using a series of requirements applied to particle-level objects, analogous to those used in the selection of the detector-level objects, described above.

Electrons and muons are required not to originate from a hadron in the MC truth record, whether directly or through a τ decay. This ensures that the lepton is from an electroweak decay without requiring a direct W-boson match. The four-momenta of the bare leptons are then modified (dressed) by adding the four-momenta of all photons within a cone of size $\Delta R = 0.1$, to take into account final-state photon radiation. Dressed electrons are then required to have $p_{\mathrm{T}} > 15$ GeV and $|\eta| < 1.37$ or $1.52 < |\eta| < 2.47$. Dressed muons are required to have $p_{\mathrm{T}} > 15$ GeV and $|\eta| < 2.5$.

Particle-level jets are reconstructed using the same anti-k_t algorithm used at detector level. The jet-reconstruction procedure takes as input all stable particles, except for charged leptons not from hadron decays as described above, inside a radius $R = 0.4$. Particle-level jets are required to have $p_{\mathrm{T}} > 25$ GeV and $|\eta| < 2.5$. A jet is identified as a b-jet if a hadron containing a b-quark is matched to the jet using the ghost-association procedure; the hadron must have $p_{\mathrm{T}} > 5$ GeV.

The simulated top-quark four-momenta are recorded after parton shower but before decays are simulated, and correspond to the parton-level description of the event. The full phase-space is defined by the set of $t\bar{t}$ pairs in which both top quarks decay hadronically. The measurements presented in this paper cover the entire phase-space.

5 Event selection and reconstruction

After events have been selected by the trigger, a series of selection criteria are applied to define a signal region (SR) containing a pure sample of resolved all-hadronic top-quark pair events. First, events are removed if detector defects or data corruption are identified, or if the events do not contain a primary vertex with at least two associated tracks. Events must contain at least six jets with $p_{\mathrm{T}} > 55$ GeV and $|\eta| < 2.4$ to be in a regime where the trigger fires with high efficiency. Exactly two b-tagged jets must be found. A veto is applied on events containing at least one electron or muon with $p_{\mathrm{T}} > 15$ GeV, or a τ-jet with $p_{\mathrm{T}} > 25$ GeV.

Subsequently, a $t\bar{t}$ reconstruction procedure is implemented, to suppress backgrounds from multi-jet production and to calculate the observables to be measured (see Section 7).

5.1 Kinematic reconstruction of the $t\bar{t}$ system

The identification of two top-quark candidates from the many jets in the event is a combinatorially complex problem. Each b-jet is assigned to one top-quark candidate, and permutations are formed for each set of four jets, selected from the remaining jets in the event. These four "light" jets are paired-up to form W-boson candidates and each W candidate is, in turn, matched with one of the b-jets to form a top-quark candidate. For the W-boson pairings and $b-W$ pairings, all unique permutations are considered. A chi-square (χ^2) discriminant is computed for each permutation to judge whether the considered permutation is compatible with the hypothesis of a top-quark pair; the permutation with the smallest chi-square χ^2_{min} is chosen as the one best describing the event as production of a top-quark pair decay.

The χ^2 discriminant is defined as:

$$\chi^2 = \frac{(m_{b_1 j_1 j_2} - m_{b_2 j_3 j_4})^2}{\sigma_t^2} + \frac{(m_{j_1 j_2} - m_W)^2}{\sigma_W^2} + \frac{(m_{j_3 j_4} - m_W)^2}{\sigma_W^2}, \tag{1}$$

where $m_{t,1} = m_{b_1 j_1 j_2}$ and $m_{t,2} = m_{b_2 j_3 j_4}$ are the invariant masses of the jets associated with the decay products of the leading and sub-leading top quark, sorted in p_{T}, respectively.[2] Similarly, $m_{j_1 j_2}$ and $m_{j_3 j_4}$ are the invariant masses of the jets associated with the decay products of the W bosons from the top quarks. The W-boson mass is taken to be $m_W = 80.4$ GeV [68]. Finally, $\sigma_t = 10.7$ GeV and $\sigma_W = 5.9$ GeV respectively represent the resolutions on the top quark and W-boson masses assuming the correct jet matching, as determined in simulated $t\bar{t}$ events in which the jet assignments were fixed unambiguously by matching jets to decay partons. The χ^2 minimisation successfully matches all jets to top decay partons in approximately 60% of $t\bar{t}$ events with exactly 6 jets, while combinatorial confusion in events with up to three additional jets can cause the matching to degrade by 10-20%.

5.2 Multi-jet background rejection

The χ^2_{min} is used as a first discriminant to reject background events; multi-jet events produce larger χ^2_{min} values, hence events are rejected if they have $\chi^2_{\text{min}} > 10$. In addition, the mass of the two reconstructed top quarks is required to be in the range $130 < m_{t,1}, m_{t,2} < 200$ GeV.

The top-antitop quarks are normally produced back-to-back in the transverse plane, hence the two b-tagged jets are produced at large angles. In contrast, the dominant mechanism for producing b-jets in background multi-jet events is $g \to b\bar{b}$ which typically results in collinear b-jets. Therefore the ΔR distance between the two b-jets, ΔR_{bb}, is required to be larger than 2. Similarly, the larger of the two angles between a b-tagged jet and its associated W boson, $\Delta R_{bW}^{\text{max}}$, has good discriminating power due to the tendency for the top-quark decay products to be slightly collimated, thus the requirement $\Delta R_{bW}^{\text{max}} < 2.2$ is imposed.

Table 2 summarises the selection criteria defining the signal region at reconstruction level. The fiducial phase space used for unfolding to particle level is defined by the same selections, with two exceptions. First, no trigger selection need be applied, as the six-jet selection ensures full efficiency. Second, in place of the b-tagging requirements, the truth b-hadron labelling is used, as described in Section 4.2.

In the data, 44 573 events pass the full event selection. The signal purity is predicted to be 68% for the nominal all-hadronic $t\bar{t}$ sample, with an uncertainty of 8.4%.

[2] In this paper, "leading", "sub-leading" *etc.* are always taken to refer to p_{T}-ordering, for brevity.

Requirement	Event selection
Multi-jet trigger	6 jets, $p_{\mathrm{T}} > 45$ GeV
Exactly 0 isolated leptons	μ: $p_{\mathrm{T}} > 15$ GeV, $\lvert\eta\rvert$<2.5 e: $p_{\mathrm{T}} > 15$ GeV, $\lvert\eta\rvert$<2.47, excluding 1.37<$\lvert\eta\rvert$<1.52 τ: $p_{\mathrm{T}} > 25$ GeV, $\lvert\eta\rvert$<2.5
At least 6 jets	6 leading jets: $p_{\mathrm{T}} > 55$ GeV Subleading jets: $p_{\mathrm{T}} > 25$ GeV
Exactly 2 b-jets	b-tagging at 70% efficiency
Top mass	130 GeV $< m_{t,1}, m_{t,2} <$ 200 GeV
Reconstructed χ^2_{min}	$\chi^2_{\mathrm{min}} < 10.0$
ΔR between b-jets	$\Delta R_{\mathrm{bb}} > 2.0$
Maximum ΔR between b-jet and W	$\Delta R^{\mathrm{max}}_{\mathrm{bW}} < 2.2$

Table 2: Summary of selection requirements.

6 Background estimation

The signal region of the resolved all hadronic topology is contaminated by two major sources of background, as shown in Table 6. The contribution of top-quark pair production decaying to non-hadronic final states is expected to be 5% of the selected all-hadronic prediction and 3% of the total data yield. The non-hadronic contribution is estimated using the same MC simulated samples as for the signal, but filtering instead for at least one leptonic W decay. The total single-top-quark contribution was estimated to be below 2% of the selected data and well within both MC and data statistical error. For this reason it is not considered further.

Multi-jet production forms the most significant source of background contamination at about a third of the total selected number of events. This is estimated using a data-driven procedure, as described below.

6.1 Data-driven estimate of multi-jet background

The estimate of the multi-jet background component is performed using the "ABCD Method", which can be applied whenever two variables exist that each provide good signal–background discrimination, while their distributions in the background process are uncorrelated. A similar method was used in previous measurements [17, 69]. The best performing pair of discriminating variables were found to be the b-jet multiplicity ($N_{\text{b-jets}}$) and a combination of the two top-quark-candidate masses. The masses of the two top-quark candidates are used to define two different mass regions as described in Table 3.

Mass region	Condition
Tail	At least one top quark with $m_t < 120$ GeV or $m_t > 250$ GeV
Peak	Both top quarks have 130 GeV $< m_t <$ 200 GeV

Table 3: Definition of the mass region based on the m_t of the two top quark candidates.

The two variables identify six different regions as shown in Table 4. The region corresponding to the signal region is region D, defined by $N_{\text{b-jets}} = 2$ and 130 GeV $< m_t <$ 200 GeV for both top quark candidates, together with the other criteria in Table 2. Background control regions are defined by a lower b-jet multiplicity and/or in the sidebands of the top-quark candidate mass distribution. In the control regions, at least one top-quark candidates must satisfy $m_t < 120$ GeV or $m_t > 250$ GeV. Excluding events where one top-quark candidate is in the signal region mass window and the other falls in either of the intermediate ranges 120 GeV $< m_t <$ 130 GeV or 200 GeV $< m_t <$ 250 GeV strongly reduces the signal contamination in the control regions with a negligible increase in the total statistical uncertainty (at 1% level), improving the overall robustness of the estimate.

	Tail	Peak
$N_{\text{b-jets}} = 0$	A_0	B_0
$N_{\text{b-jets}} = 1$	A_1	B_1
$N_{\text{b-jets}} = 2$	C	D

Table 4: Division into orthogonal regions according to the $N_{\text{b-jets}}$ parameter and a combination of the two top-quark masses as defined in Table 3.

The background estimate is carried out for each bin in the measured distributions. The differential background estimate D in one bin of a generic observable X is defined as:

$$D(X) = \frac{B_1(X) \cdot C(X)}{A_1(X)}, \tag{2}$$

where the control region background yields $\{A_1, B_1, C\}$ are determined by subtracting the MC $t\bar{t}$ predictions (of all decay modes) from the data yields in each region.

A parallel estimate D' is made using regions A_0 and B_0 to assess the systematic uncertainty of the method, which accounts for potential differences in the kinematic properties for the various flavour components of the multi-jet background. This is defined as:

$$D'(X) = \frac{B_0(X) \cdot C(X)}{A_0(X)}, \tag{3}$$

such that $\Delta D = D' - D$ gives the systematic uncertainty on the nominal prediction D.

Table 5 shows the fraction of signal and background $t\bar{t}$ events estimated from MC in the various regions. More signal contamination is observed in regions with b-tagged jets, but sufficient background purity is observed in all regions such that signal mismodelling should not substantially bias the background prediction.

The spectra of observables used to define the signal region, namely χ^2_{min}, ΔR_{bb} and $\Delta R^{\text{max}}_{bW}$ are presented in Figure 1. These plots are done in an "$N - 1$" requirement configuration; the plot for a particular variable

Region	Definition	All-hadronic $t\bar{t}$/Data	Non all-hadronic $t\bar{t}$/Data
A_0	$N_{\text{b-jets}} = 0$ tail	1.87 %	0.19 %
B_0	$N_{\text{b-jets}} = 0$ peak	0.96 %	0.08 %
A_1	$N_{\text{b-jets}} = 1$ tail	3.35 %	0.69 %
B_1	$N_{\text{b-jets}} = 1$ peak	16.10 %	1.16 %
C	$N_{\text{b-jets}} = 2$ tail	16.14 %	2.90 %
D	$N_{\text{b-jets}} = 2$ peak	66.09 %	3.35 %

Table 5: Fractional yields from top-quark pair production processes in the different regions, defined by the values assumed by $N_{\text{b-jets}}$ and the two top quarks m_t as defined in Table 3.

is made after applying all signal region requirements except that on the variable being displayed. The $m_{t,1}$ and $m_{t,2}$ spectra are not shown since those observables are used to define the control regions in the multi-jet estimation.

Although the total predictions do not perfectly reproduce the data distributions everywhere they are compatible with data within the total uncertainties, given for illustrative purposes by the sum of statistical and dominant systematic components. The dominant source of uncertainties in the six-jet case is the $t\bar{t}$ theoretical modelling (parton shower and initial-state radiation), whereas the systematic uncertainty on the multi-jet estimate dominates the inclusive jet distributions. Together, the comparisons indicate an adequate description of the signal and background processes.

The event yields after this selection are shown in Table 6 for data, simulated MC signal and background (as estimated following the procedure described in Section 6).

Process	Event yield	Fraction (%)
$t\bar{t}$ (all-hadronic)	$29\,500\,^{+2000}_{-2500}$	68%
$t\bar{t}$ (non all-hadronic)	$1490\,^{+140}_{-120}$	3%
Multijet background	$12\,600\,^{+1900}_{-1900}$	29%
Total prediction	$43\,500\,^{+2800}_{-3000}$	
Data	44 573	

Table 6: Event yields for data, signal and background processes after the signal region selection. Uncertainties are quoted as the sum in quadrature of statistical and detector-level systematic uncertainties. The composition of the selected events is also given in terms of the fractional contribution of the signal and background processes to the total yield.

Figure 2 shows the jet multiplicity distribution for selected events in data compared to the total SM prediction. This demonstrates that the 6-jet bin is essentially pure $t\bar{t}$, with negligible background contamination, and in fact the nominal signal MC slightly exceeds the data yield. In higher jet multiplicity bins the combinatorial difficulty for correctly identifying the jets from the top-quark decays increases, resulting in a growing multi-jet background contribution.

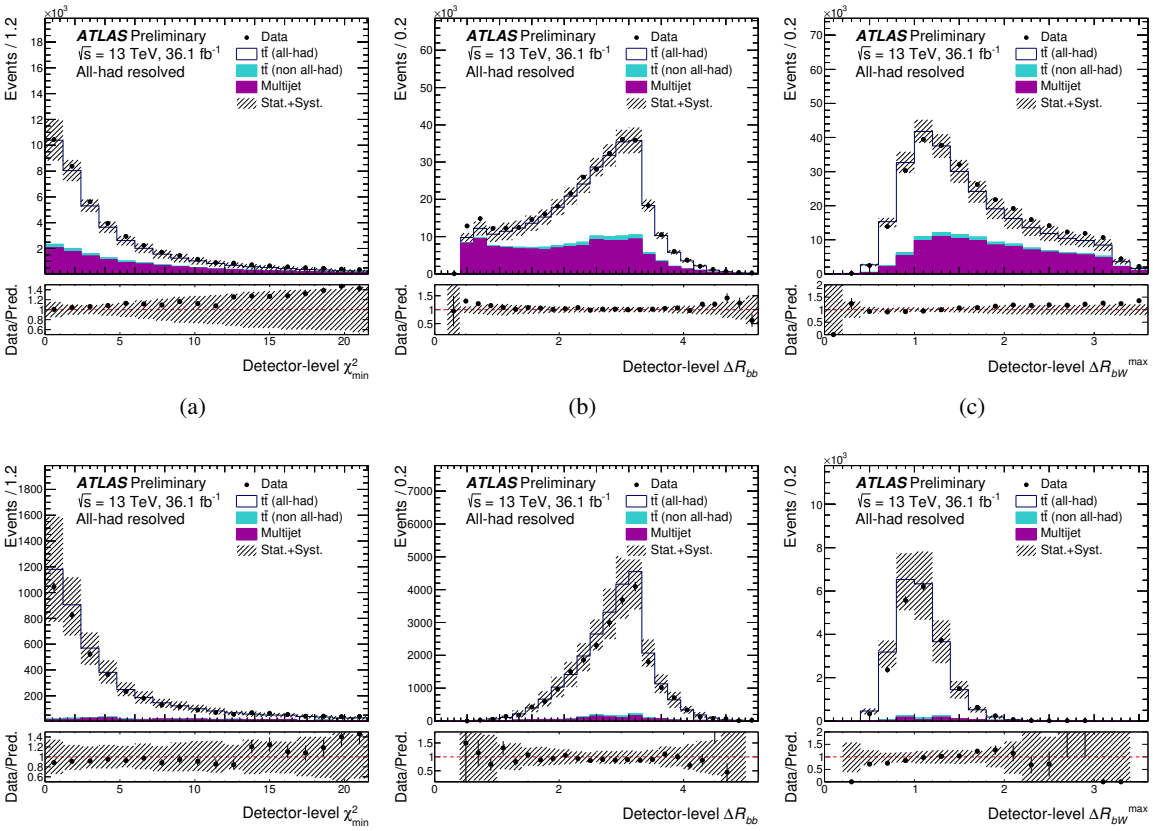

Figure 1: Detector-level distributions in the signal regions as a function of the (left) χ^2_{min}, (middle) ΔR_{bb} and (right) $\Delta R_{bW}^{\text{max}}$, for (top) all selected events and (bottom) exclusive six-jet events. The signal prediction is based on the POWHEG+PYTHIA8 generator. The background is the sum of the data-driven multi-jet estimate and the MC-based expectation for the contributions of non all-hadronic $t\bar{t}$ production process. Statistical uncertainties combined with the dominant systematics for the applied selection are shown in hatching. In the inclusive N_{jets} selection, only the systematic uncertainty on the multi-jet background estimate is included, while for the six-jet selection only the $t\bar{t}$ modelling uncertainties are considered.

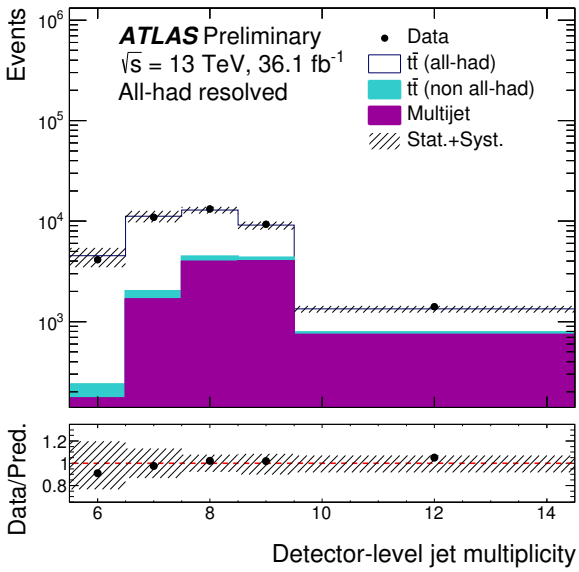

Figure 2: Jet multiplicity in the SR. The signal prediction is based on the POWHEG+PYTHIA8 generator. The background is the sum of the data-driven multi-jet estimate (purple histogram) and the MC-based expectation for the contributions of non-all-hadronic $t\bar{t}$ production process (light blue histogram). Statistical uncertainties combined with relevant systematics are shown in hatching.

7 Observables

In the analysis described in this paper, the differential cross-sections are measured as a function of a variety of observables sensitive to the kinematics of top-quark pair production and accompanying radiation. The all-hadronic final state makes each of the top-quark decay products visible, making it especially suited to determining the kinematics of the individual top quarks and of the $t\bar{t}$ system. These variables rely on the reconstruction of the $t\bar{t}$ system, which is described in Section 5.1.

7.1 Single-differential cross-section measurements

In the following subsections, the observables used to measure the single-differential cross-sections are described.

7.1.1 Kinematic observables of the top quarks and $t\bar{t}$ system

A set of baseline observables is presented. These variables describe the characteristic features of the four-momentum of the individual top quarks and the $t\bar{t}$ system. The cross-section is measured both at particle and at parton level as a function of the transverse momentum ($p_{\mathrm{T}}^{t,1}$ and $p_{\mathrm{T}}^{t,2}$) and absolute value of rapidity ($|y^{t,1}|$ and $|y^{t,2}|$) of the leading and sub-leading top quarks. For the $t\bar{t}$ system the transverse momentum ($p_{\mathrm{T}}^{t\bar{t}}$), the absolute value of rapidity ($|y^{t\bar{t}}|$) and mass ($m^{t\bar{t}}$) are measured.

In addition, differential cross-sections as a function of the observables listed below are measured. These variables extend the information on the properties of the $t\bar{t}$ system and they are sensitive to more than one aspect of the $t\bar{t}$ production:

- $H_{\mathrm{T}}^{t\bar{t}}$: the scalar sum of the p_{T} of the two top quarks;
- $|y_{\mathrm{boost}}^{t\bar{t}}|$: $|y^{t,1}-y^{t,2}|/2$ the absolute value of the average rapidity of the two top quarks;
- $\chi^{t\bar{t}}$: $\exp(|y^{t,1}-y^{t,2}|)$, which gives sensitivity to small rapidity differences between the top quarks.

The $|y_{\mathrm{boost}}^{t\bar{t}}|$ observable is expected to be sensitive to the PDF description, while the $\chi^{t\bar{t}}$ variable is of particular interest as many processes not included in the SM are predicted to peak at low values of $\chi^{t\bar{t}}$ [17, 70].

Differential cross-sections as a function of another set of observables are measured at particle level, such that they may be used to constrain the modelling of the direction and the p_{T}-sharing of the top quarks and their decay products by various matrix element and parton shower MC generators. These observables comprise directional observables and transverse momentum ratios, as listed below:

- $\Delta\phi^{t\bar{t}}$: the angular distance in ϕ between top quarks;
- $|P_{\mathrm{cross}}^{t\bar{t}}|$: $\left|[\hat{b_1}\times(\hat{j_1}\times\hat{j_2})]\times[\hat{b_2}\times(\hat{j_3}\times\hat{j_4})]\right|$ cross products of the jets directions;
- $|P_{\mathrm{out}}^{t,1}|$: $\left|\vec{p}^{\,t,1}\cdot\frac{\vec{p}^{\,t,2}\times\hat{z}}{|\vec{p}^{\,t,2}\times\hat{z}|}\right|$ out-of-plane momentum defined as the projection of the top-quark three-momentum onto the direction perpendicular to the plane defined by the other top quark and the beam axis ($\hat{z}$) in the laboratory frame [71];
- $Z^{t\bar{t}}$: the p_{T} ratio of the sub-leading to the leading top quark;

- R_{Wt}: p_{T} ratio of W boson to its associated top quark (leading and sub-leading);
- R_{Wb}: p_{T} ratio of W boson to its associated b-quark (leading and sub-leading);

These observables were first studied in the 8 TeV ℓ+jets differential cross-section measurement [13] and were also included in the hadronic di-boosted measurement at 13 TeV [17]. By repeating these measurements in the resolved channel it is possible to complement the results of the latter publication. Furthermore, the channel used in the analysis described in this paper does not have neutrinos in the final state, avoiding the dependency on the $E_{\mathrm{T}}^{\mathrm{miss}}$, whose resolution is affected by all measured jets in the event. Hence, a good resolution is achieved on all directional observables such as $|P_{\mathrm{out}}^{t,1}|$, $\chi^{t\bar{t}}$ and $\Delta\phi^{t\bar{t}}$. Given that four-momenta are available for all visible decay products, a new variable was introduced using only the direction of the jets which is called $P_{\mathrm{cross}}^{t\bar{t}}$, for which the magnitude will be measured.

7.1.2 Jet observables

A set of jet-related observables is presented, unfolded at particle level in the fiducial phase space. The differential cross-section is measured as a function of the number of reconstructed jets (N_{jets}). In addition, a set of observables sensitive to the angular and energy correlations between the additional jets and the top quarks is listed below. The additional jets are those jets that are not associated with either top quark by the reconstruction procedure. The closest top quark refers to the top candidate with a smaller ΔR separation to the jet in question:

- ΔR between the leading, sub-leading, sub-subleading extra jet and the closest top quark, denoted $\Delta R_{t,\mathrm{close}}^{\mathrm{extra1}}$, $\Delta R_{t,\mathrm{close}}^{\mathrm{extra2}}$, $\Delta R_{t,\mathrm{close}}^{\mathrm{extra3}}$;
- p_{T} ratio between the leading, sub-leading, sub-subleading extra jet and the leading top quark, denoted $R_{t,1}^{\mathrm{extra1}}$, $R_{t,1}^{\mathrm{extra2}}$, $R_{t,1}^{\mathrm{extra3}}$;
- p_{T} ratio between the leading, sub-leading, sub-subleading extra jet and the leading jet, denoted $R_{\mathrm{jet1}}^{\mathrm{extra1}}$, $R_{\mathrm{jet1}}^{\mathrm{extra2}}$, $R_{\mathrm{jet1}}^{\mathrm{extra3}}$;
- p_{T} ratio between the $p_{\mathrm{T}}^{t\bar{t}}$and leading extra jet, denoted $R_{\mathrm{extra1}}^{t\bar{t}}$.

The ΔR is taken with respect to the closest top quark, as collinear emissions are favoured, and furthermore the sub-leading top quark is more likely to have lost momentum via a hard emission. The first p_{T} ratio uses the leading top quark as a reference for the hard scale in the event, while the second is sensitive to emissions beyond the first, in particular soft gluons that may not be resolved as jets, allowing a test of resummation effects.

Further constraints can be placed on correlations between the angles and between the transverse momenta of additional jets themselves, which are particularly of interest for multileg matrix element calculations, by measuring differential cross-sections as a function of the following observables:

- ΔR between the leading extra jet and the leading jet, denoted $\Delta R_{\mathrm{jet1}}^{\mathrm{extra1}}$;
- ΔR between the sub-leading, sub-subleading extra jet and the leading extra jet, denoted $\Delta R_{\mathrm{extra1}}^{\mathrm{extra2}}$, $\Delta R_{\mathrm{extra1}}^{\mathrm{extra3}}$;
- p_{T} ratio between the sub-leading, sub-subleading extra jet and the leading extra jet, denoted $R_{\mathrm{extra1}}^{\mathrm{extra2}}$, $R_{\mathrm{extra1}}^{\mathrm{extra3}}$.

Because ISR scales with the partonic centre-of-mass energy, when the leading extra jet is the hardest object in the event its transverse momentum serves well as a reference for the energy scale of the interaction.

7.2 Double differential measurements

The observables described below are used to perform double-differential measurements at both particle and parton level. The measurements of these observables allow finer understanding of correlations between different aspects of the $t\bar{t}$ system kinematics. These combinations are useful to extract information about PDFs and measure the top-quark pole mass from the differential cross-section measurements. The combinations considered are:

- $p_{\mathrm{T}}^{t,1}$, $p_{\mathrm{T}}^{t,2}$, $|y^{t,1}|$, $|y^{t,2}|$, $p_{\mathrm{T}}^{t\bar{t}}$ and $\left|y^{t\bar{t}}\right|$ in bins of $m^{t\bar{t}}$;
- $p_{\mathrm{T}}^{t,1}$ in bins of $p_{\mathrm{T}}^{t,2}$;
- $|y^{t,1}|$ in bins of $|y^{t,2}|$.

Additional observables are measured differentially at particle level only as a function of the jet multiplicity which can be used to tune and constrain the parameters of MC generators. The combinations considered are:

- $p_{\mathrm{T}}^{t,1}$, $p_{\mathrm{T}}^{t,2}$, $p_{\mathrm{T}}^{t\bar{t}}$, $|P_{\mathrm{out}}^{t,1}|$, $\Delta\phi^{t\bar{t}}$ and $|P_{\mathrm{cross}}^{t\bar{t}}|$ in bins of N_{jets}.

8 Unfolding strategy

The measured differential cross-sections are obtained from the reconstruction-level distributions using an unfolding technique which corrects for detector and reconstruction effects such as efficiency, acceptance and resolution. The iterative Bayesian unfolding method [72] as implemented in RooUnfold [73] is used.

For each observable, the unfolding procedure starts from the number of events observed in data at reconstruction level in bin j of the distribution N_{obs}^{j}, from which the background event yield N_{bkg}^{j}, estimated as described in Section 6, is subtracted. Then the corrections are applied. All corrections are evaluated using the MC simulation of the signal $t\bar{t}$ sample.

8.1 Unfolding at particle level

As the first step, an acceptance correction is applied. The acceptance correction in bin j is defined as the fraction of signal events reconstructed in this bin that also pass the particle-level selection:

$$f_{\mathrm{acc}}^{j} \equiv \frac{N_{\mathrm{reco}\wedge\mathrm{part}}^{j}}{N_{\mathrm{reco}}^{j}}. \tag{4}$$

This correction is a bin-by-bin factor which corrects for events that are generated outside the fiducial phase-space region but pass the reconstruction-level selection. The resulting distribution is then unfolded to the particle or parton level.

The unfolding step uses as input a migration matrix ($\mathcal{M}$) derived from simulated $t\bar{t}$ samples which maps between the particle-level bin i in which an event falls to the bin j in which it is reconstructed. The probability for particle-level events to be reconstructed in the same bin is therefore represented by the elements on the diagonal, and the off-diagonal elements describe the fraction of particle-level events that migrate into other bins. Therefore, the elements of each row sum to unity (within rounding). For each observable, the number of bins is optimised to maximise information extraction under stable unfolding conditions, based on the resolution of the ATLAS detector and reconstruction algorithms.

The unfolding is performed using four iterations to balance the unfolding stability with respect to the previous iteration and the growth of the statistical uncertainty, which is limited to be below 0.1%.

Finally, an efficiency correction (ϵ) is applied to the unfolded spectrum, correcting the result by a bin-by-bin factor to the fiducial phase space, defined in Section 5. The efficiency correction in bin i is defined as the fraction of the events generated in a particle-level bin i that pass the inclusive reconstruction-level selection:

$$\epsilon^i \equiv \frac{N^i_{\text{part}\wedge\text{reco}}}{N^i_{\text{part}}}. \tag{5}$$

This factor corrects for the inefficiency of the event selection and reconstruction.

As an example, Figure 3 shows the corrections and the migration matrix for the case of the p_{T} of the leading top quark.

The extraction of the absolute differential cross-section for an observable X at particle level is then summarised by the following expression:

$$\frac{\mathrm{d}\sigma^{\text{fid}}}{\mathrm{d}X^i} \equiv \frac{1}{\mathcal{L}\cdot\Delta X^i}\cdot\frac{1}{\epsilon^i}\cdot\sum_j \mathcal{M}^{-1}_{ij}\cdot f^j_{\text{acc}}\cdot\left(N^j_{\text{obs}} - N^j_{\text{bkg}}\right), \tag{6}$$

where the index j iterates over bins of observable X at reconstruction level while the index i labels bins at particle level; ΔX^i is the bin width while $\mathcal{L}$ is the integrated luminosity, and the inverted migration matrix as obtained with the iterative unfolding procedure is symbolised by $\mathcal{M}^{-1}_{ij}$. The integrated fiducial cross section is obtained by integrating the unfolded cross section over the bins, and its value is used to compute the normalised differential cross-sections:

$$\frac{1}{\sigma^{\text{fid}}}\cdot\frac{\mathrm{d}\sigma^{\text{fid}}}{\mathrm{d}X^i}. \tag{7}$$

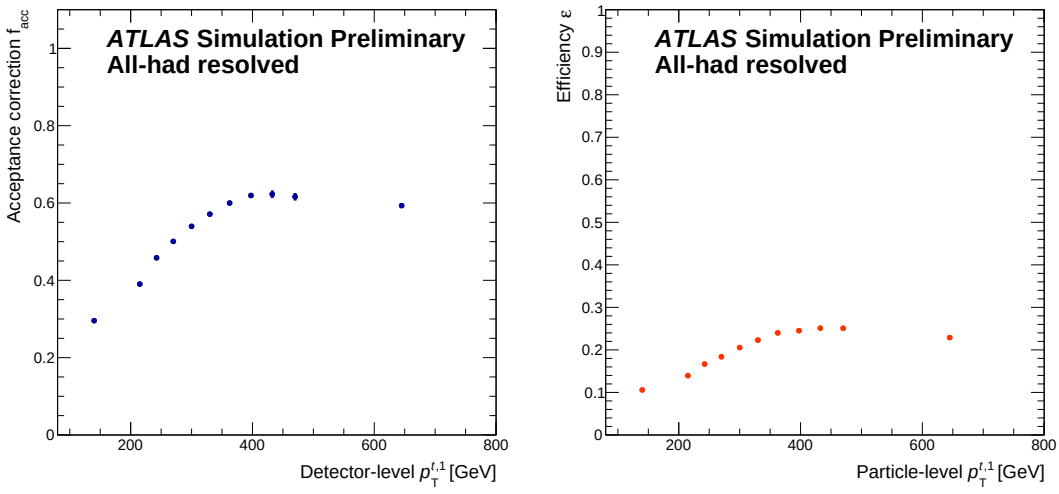

(a)

(b)

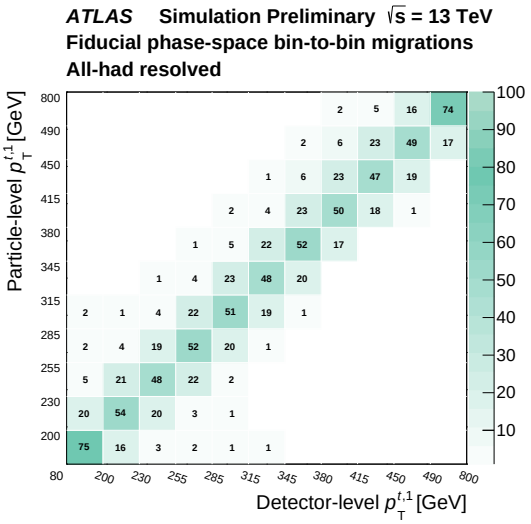

(c)

Figure 3: The (a) acceptance f_{acc}, and (b) efficiency ϵ corrections binned to detector- and particle-level p_{T} respectively, and the (c) particle-to-detector-level migration matrix (evaluated with the MC $t\bar{t}$ signal sample) for the transverse momentum of the leading top quark.

8.2 Unfolding at parton level

The measurements are extrapolated to the full phase space of the $t\bar{t}$ system using the same procedure as for extrapolation to the fiducial phase space. The binning is re-optimised due to the different resolution; this leads to similar migration matrices. Since in this case the measurements are unfolded to the full phase space, the acceptance correction is irrelevant, however large efficiency corrections are needed due to the larger extrapolation.

As an example, Figure 4 shows the efficiency corrections and the migration matrix for the case of the p_{T} of the leading top quark.

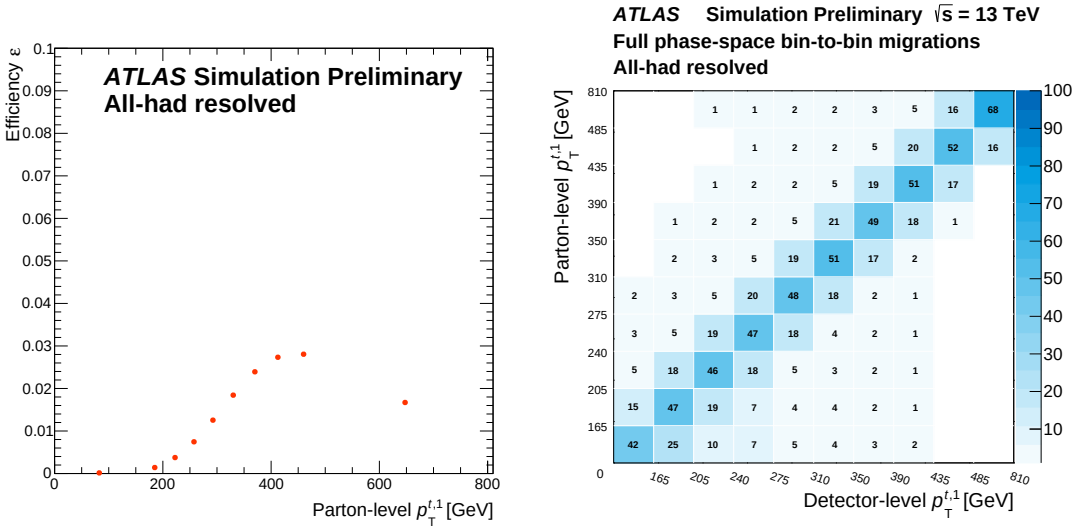

(a) (b)

Figure 4: The (a) efficiency ϵ corrections in bins of the parton-level p_{T} respectively and the (b) parton-to-detector-level migration matrix (evaluated with the MC $t\bar{t}$ signal sample) for the transverse momentum of the leading top quark. The acceptance correction f_{acc} is identically 1, and therefore not displayed.

The unfolding procedure is summarised by the following expression:

$$\frac{\mathrm{d}\sigma^{\mathrm{full}}}{\mathrm{d}X^i} \equiv \frac{1}{\mathcal{L}\cdot\mathcal{B}\cdot\Delta X^i}\cdot\frac{1}{\epsilon^i}\cdot\sum_j \mathcal{M}_{ij}^{-1}\cdot\left(N_{\mathrm{obs}}^j - N_{\mathrm{bkg}}^j\right), \tag{8}$$

where the index j iterates over bins of observable X at reconstruction level while the index i labels bins at the parton level; ΔX^i is the bin width, $\mathcal{B} = 0.456$ is the all-hadronic branching ratio, $\mathcal{L}$ is the integrated luminosity, and the inverted migration matrix as obtained with the iterative unfolding procedure is symbolised by $\mathcal{M}_{ij}^{-1}$.

9 Systematic uncertainties

Several sources of systematic uncertainties affect the measured differential cross-sections. The systematic uncertainties due to detector effects and the ones related to the modelling of the signal and background MC components are found to be the most relevant, compared to uncertainties on the unfolding procedure.

Each systematic uncertainty was evaluated before and after the unfolding procedure (described in Section 8). Deviations from the nominal predictions were evaluated separately for the upward and downward variations (or in the case of a single variation by symmetrising the single deviation) for each bin of each observable.

In the absence of backgrounds, the uncertainty on the predictions (ΔS_{syst}) would be evaluated as the difference between the nominal and alternative MC signal samples using the formula $\Delta S_{\mathrm{syst}} = S_{\mathrm{syst}} - S_{\mathrm{nominal}}$.

To account for the effect of the uncertainties on the background yields, the total predictions (T) need to be compared instead: $\Delta S_{\text{syst}} = T_{\text{syst}} - T_{\text{nominal}}$. The total predictions, for both nominal and systematically varied samples, are given by the sum of the all-hadronic signal sample, the non-all-hadronic contribution and by the multi-jet background estimated with those samples. Hence, for the estimate of the uncertainty on the signal modelling, the non-all-hadronic events and the multi-jet events are considered fully correlated with the all-hadronic signal sample.

The varied MC detector-level spectrum is then unfolded using the background subtraction and corrections evaluated with the nominal $t\bar{t}$ signal sample and the unfolded result is compared to the corresponding particle- or parton-level distribution. All detector- and background-related systematic uncertainties are evaluated using the nominal MC generator, while alternative event generators are employed to assess the systematic uncertainties related to the $t\bar{t}$ system modelling as described in Section 9.2. In the latter case, the corrections derived from the nominal event generator are used to unfold the detector-level spectra of the alternative event generator.

The detector-related uncertainties are briefly described in Section 9.1 while the uncertainties on the $t\bar{t}$ signal and background modelling are discussed in Sections 9.2 and 9.3 respectively.

9.1 Detector modelling

The experimental uncertainties quantify the degree to which the simulated detector response is trusted to reproduce collision data for each of the reconstructed objects as well as other empirical uncertainties on object reconstruction and calibration. For a given source of systematic uncertainty, its impact on the measurement is evaluated by replacing the nominal MC predictions for signal and non-QCD background with their systematic variations, then rerunning the QCD background estimate and unfolding the data using the nominal correction factors. Due to the selected final state, the main experimental systematics arise due to jet reconstruction and flavour tagging. As events with leptons are removed, the corresponding uncertainties are negligible.

Jet reconstruction

The uncertainty on the JES were estimated by using a combination of simulation, test beam data and *in situ* measurements. Additional contributions from jet flavour composition, η-intercalibration, punch-through, single-particle response, calorimeter response to different jet flavours and pile-up are taken into account, resulting in 29 independent sub-components of systematic uncertainty [57, 74, 75].

The uncertainty due to the difference in jet-energy resolution (JER) between the data and MC events was evaluated by smearing the MC jet transverse momentum according to the jet resolution as a function of the jet p_{T} and η [76]. Uncertainties on the efficiency of the requirement on JVT are determined from efficiency measurements made on $Z \to ee/\mu\mu$+jets events [77] and applied as variations on the jet-by-jet efficiency corrections.

b-tagging

Systematic uncertainties associated with tagging jets originating from b-quarks are separated into three categories: the efficiency of the tagging algorithm for tagging b-initiated jets, the misidentification rates for jets initiated by c-quarks and finally the misidentification rates for jets originating from light-quark flavours. These efficiencies are estimated from data and parametrised as a function of p_{T} and η [78]. Uncertainties on the efficiencies arise from factors used to correct the differences between the simulation and data in each of the categories. The uncertainties in the simulation modelling of the b-tagging performance are assessed by studying b-jets in dileptonic $t\bar{t}$ events. While the systematic uncertainties on the c-jet and light-jet tagging efficiency are generally sub-percent level, the uncertainty on b-jet tagging efficiency systematics can grow as large as 5%.

Luminosity

The uncertainty in the combined 2015+2016 integrated luminosity is 2.1% [27].

9.2 Signal modelling

The choice of MC generator used in the signal modelling affects the kinematic properties of simulated $t\bar{t}$ events, the reconstruction efficiencies and the estimate of the multi-jet background.

MC generator: matrix element and parton shower and hadronisation models

Signal and background $t\bar{t}$ events simulated with generator configurations other than the nominal were used to assess the impact of different NLO matrix element calculations, as well as those of the parton shower and hadronisation models. Consistent detector simulation is used for both nominal and systematic variations.

The uncertainty due to the choice of matrix element generator is determined by unfolding a MadGraph5_aMC@NLO+Pythia8 sample using corrections and response matrices from the nominal sample. The unfolded result is then compared to the truth-level spectrum of the MadGraph5_aMC@NLO+Pythia8 sample and the relative difference is used as the systematic uncertainty from the ME generator.

The uncertainty due to the choice of fragmentation model is determined by unfolding a Powheg+Herwig7 sample using corrections and response matrices from the nominal sample. The unfolded result is then compared to the truth-level spectrum of the Powheg+Herwig7 sample and the relative difference is used as the systematic uncertainty from the parton shower and hadronisation.

The resulting systematic uncertainties are found to depend strongly on the variable and the bin. The matrix element and parton shower variations are found to be the most significant sources of systematics and usually affect the tails of the distributions by 20% at the most, although for most distributions they amount to a few percent.

Initial-state QCD radiation

The amount of ISR changes the number of jets in the event as well as the transverse momentum of the $t\bar{t}$ system. In order to evaluate the uncertainty linked to the modelling of the ISR, $t\bar{t}$ MC samples with modified ISR modelling are used. In particular, samples generated similarly to the nominal sample are unfolded, where the factorisation and re-normalisation scales as well as the value of the h_{damp} parameter were co-varied as described in Section 3.1.

In each case, the spectrum unfolded using the nominal sample is compared to the truth-level spectrum of the corresponding ISR sample. Being at the level of a few percent for most bins, the ISR variations are at most comparable to the parton shower and matrix element uncertainties.

Parton distribution functions

The impact of the choice of different PDF sets has been assessed using the 30-eigenvector set of the PDF4LHC15 prescription [53]. The effect of a different PDF choice modifies the efficiency, acceptance and potentially also the response matrix, i.e. the corrections used to correct the spectrum at the detector level to the particle level. The PDF choice effect has been evaluated by unfolding the nominal Powheg+Pythia8 sample using differently PDF re-weighted corrections. The intra-PDF variations were combined to define a relative uncertainty as:

$$\delta_{\text{intra}} \equiv \frac{\sqrt{\sum\limits_{i \in \text{sets}} (U_i \cdot R_0 - T_0)^2}}{T_0}, \tag{9}$$

while the relative inter-PDF between the NNPDF3.0 and the PDF4LHC15 central is evaluated as:

$$\delta_{\text{inter}} \equiv \frac{U_{\text{NNPDF3.0}} \cdot R_0 - T_0}{T_0}, \tag{10}$$

where the 0 (i) subscripts denote the PDF4LHC15 central (varied) PDF set, R represents the distribution at the detector level while T symbolises the distribution at the particle level, and the unfolding procedure is represented by the U factor, with subscript on each characterizing the PDF set used to evaluate the spectrum or the corrections. The resulting uncertainties are found to be at the sub-percent level, with few excesses to 1% or 2% in small-population bins.

MC generator: sample size

To account for the limited size of the signal MC sample, pseudo-experiments are used to evaluate the impact of sample size. The event yield in each bin is generated from a Gaussian distribution with mean equal to the yield of the bin and standard deviation equal to the Poisson uncertainty on the bin yield. This smeared spectrum is then unfolded. The procedure is replicated 10000 times, then the final statistical uncertainty is evaluated as the difference between the nominal prediction and the average over the 10000 pseudo-experiments. The resulting systematic uncertainty was found to be typically below 0.5%, increasing to 1–2% in the tails of some distributions.

9.3 Background modelling

Two sources of uncertainty on the background predictions are assessed in addition to the effects of the signal modelling uncertainties on the background subtraction in the control regions. The first is related to the finite number of events used in the evaluation of the background. This uncertainty is treated in the same way as the MC sample size and is listed as multi-jet Stat in all plots. The second component represents the intrinsic error of the ABCD method used for estimating the multi-jet background. An alternative background prediction is made, substituting the 0-*b*-tag control regions for the 1-*b*-tag control regions, according to Eq. 3 and used in the background subtraction step of the unfolding. The background systematic error is given by the difference between the unfolded distributions in the two scenarios and symmetrised. For example, bins at low $p_{\mathrm{T}}^{t,2}$ have a larger background contamination and therefore suffer more from this uncertainty.

The statistical uncertainty on the multi-jet background estimation is small, usually under 5%. The systematic uncertainty is ordinarily sub-dominant to uncertainties from modelling and JES/JER, occasionally reaching 10%. In rare cases the uncertainty can be larger, but this mainly implies a low signal purity, which amplifies the effect of the background systematic uncertainty.

An assessment is also made of the impact of using a fixed total $t\bar{t}$ cross-section when computing the background prediction. In the background estimation, the normalisation is varied by the uncertainty of the inclusive cross-section, which in relative terms is 5.2%. The corresponding uncertainty on the measurement is very small, normally less than 1%, given the small contamination of the signal in the control regions.

9.4 Systematic uncertainty summary

A general overview of the dominant systematic uncertainties that affect the measurement is reported in Table 7. In the Table, the systematic uncertainties that affect the inclusive cross section measurement at both particle and parton level, grouped per type, are shown. The total cross-section measured in the fiducial phase space and compared with several MC predictions is reported in Subsection 10.3.

Looking at the Table, the dominant source of uncertainty at particle level is the contribution of the hadronisation component, followed by the contribution of the JES and JER uncertainties. The same conclusion can be drawn at parton level, were the dominant source of uncertainty is the hadronisation component followed by the uncertainty on the QCD estimation and the uncertainty on the JES and JER components.

Source	Uncertainty [%]	
	Particle level	Parton level
PS/Hadronisation	8.2	7.9
Multi-jet Syst.	7.7	7.7
JES/JER	6.7	6.7
ISR, PDF	3.3	3.5
ME Generator	2.4	5.3
Flavour Tagging	2.2	2.2
Luminosity	2.1	2.1
Multi-jet Stat.	0.6	0.6
MC Signal Stat.	0.3	0.3
Stat. Unc.	0.7	0.7
Stat+Syst Unc.	14	15

Table 7: Summary of the main relative uncertainties on the inclusive cross-section measured at particle and parton level. The uncertainties are symmetrised.

10 Results

In this section, the measurements of the differential cross-sections are reported. First, the overall agreement between the measurements and various theoretical predictions are shown in the form of χ^2 tables. A more detailed discussion of the modelling of individual observables follows. Finally, comparisons are made between the results of this analysis and other measurements of specific observables.

10.1 Overall assessment of data-MC agreement

The agreement between the measured differential cross-sections and the theoretical predictions is quantified by calculating χ^2 values. These are evaluated using the total covariance matrices of the uncertainties on the measurement; the uncertainties in the theoretical predictions are not included in this evaluation. The χ^2 is given by the following relation:

$$\chi^2 = V_{N_\mathrm{b}}^\mathrm{T} \cdot \mathrm{Cov}_{N_\mathrm{b}}^{-1} \cdot V_{N_\mathrm{b}}\,, \tag{11}$$

where N_b is the number of bins of the spectrum and V_{N_b} is the vector of differences between the measured and predicted cross sections. $\mathrm{Cov}_{N_\mathrm{b}}$ represents the covariance matrix. The p-values (probabilities that the χ^2 is larger than or equal to the observed value) are then evaluated from the χ^2 and the number of degrees of freedom (NDF), which is equal to N_b. The total covariance matrix including the effect of all uncertainties is obtained by summing two covariance matrices.

The first covariance matrix incorporates the statistical uncertainty and the systematic uncertainties from detector and background modelling. It is obtained by performing pseudo-experiments where, in each pseudo-experiment, each bin of the data distribution is varied following a Poisson distribution. Gaussian-distributed shifts are coherently added for each systematic uncertainty by scaling each Poisson-fluctuated bin with the relative variation from the associated systematic uncertainty effect.

If the number of events in a given bin of a pseudo-experiment becomes negative due to the effect of the combined systematic shifts, this value is set to zero before the unfolding stage. Differential cross sections are obtained by unfolding each varied reconstructed distribution with the nominal corrections, and the results are used to compute the first covariance matrix.

The second covariance matrix is obtained by summing four separate theory-model covariance matrices corresponding to the effects of the $t\bar{t}$ generator, parton shower/hadronisation, ISR and PDF uncertainties. Elements of these covariance matrices are computed by multiplying the relative systematic uncertainties scaled by the measured cross section in each bin. The bin-to-bin correlation value is set to unity for each contribution. This procedure is needed for the signal modelling uncertainties because they cannot be represented as smooth variations at detector level, and so cannot be included in the pseudo-experiment formalism used for the first covariance matrix.

To compare only the shapes of the measured cross-sections and the predictions, the results are also presented as normalised cross-sections. This treatment reduces the contribution of uncertainties common to all bins of the distributions, highlighting shape differences relative to the absolute case. For normalised differential cross-sections, V_{N_b} is replaced with $V_{N_\mathrm{b}-1}$, which is the vector of differences between data and prediction obtained by discarding the last one of the N_b elements and, consequently, $\mathrm{Cov}_{N_\mathrm{b}-1}$ is the $(N_\mathrm{b}-1)\times(N_\mathrm{b}-1)$ sub-matrix derived from the full covariance matrix discarding the corresponding row and column. The sub-matrix obtained in this way is invertible and allows the χ^2 to be computed. The χ^2 value does not depend on the choice of the element discarded for the vector $V_{N_\mathrm{b}-1}$ and the corresponding sub-matrix $\mathrm{Cov}_{N_\mathrm{b}-1}$. In this case, the NDF becomes $N_b - 1$.

The χ^2 values and their corresponding p-values are reported below for differential cross-sections measured at particle level in the fiducial phase space (Section 10.1.1) and at parton level in the full phase space (Section 10.1.2). All observables introduced in Section 7 are included in these tables.

10.1.1 Cross-sections in the fiducial phase space

The quantitative comparisons among the single-differential particle-level results and theoretical predictions are shown in Tables 8 and 9. Overall, the MC generator that gives the best description of several single-differential distributions is Powheg+Herwig7, followed by Powheg+Pythia8. Other predictions are less accurate, with MadGraph5_aMC@NLO+Pythia8 and the Powheg+Pythia8 Var3cDown variation giving the poorest agreement. Some variables that are generally well described by all the MC generators show a mismodelling with only one of the available MC generators: this is the case of the $\Delta R^{\mathrm{extra2}}_{\mathrm{extra1}}$observable, where Powheg+Herwig7 shows a poorer agreement with data, while, for the absolute measurements of the $\Delta\phi^{t\bar{t}}$ and $Z^{t\bar{t}}$ observables, the MadGraph5_aMC@NLO+Pythia8 is the only sample that shows a disagreement with the data.

Conversely, it is noted that $R^{\mathrm{leading}}_{Wt}$ is not well described by any MC prediction while $R^{\mathrm{extra3}}_{\mathrm{extra1}}$ is only described accurately by MadGraph5_aMC@NLO+Pythia8. The two top-quark p_T observables are only described correctly by Powheg+Herwig7 and Powheg+Pythia8 Var3cUp predictions while the Powheg+Pythia8 Var3cDown prediction shows the poorest agreement for these observables.

The results of the double-differential cross-sections are shown in Tables 10 and 11 and demonstrate a larger difference between MC predictions. Again, Powheg+Herwig7 gives the best agreement overall, although it does not provide adequate descriptions for a few variables. MadGraph5_aMC@NLO+Pythia8 and Powheg+Pythia8 Var3cDown have the poorest agreement among all MC predictions.

Observable	PWG+PY8		PWG+PY8 Var. Up		PWG+PY8 Var. Down		aMC@NLO+PY8		Sherpa		PWG+H7	
	χ^2/NDF	p-value	χ^2/NDF	p-value	χ^2/NDF	p-value	χ^2/NDF	p-value	χ^2/NDF	p-value	χ^2/NDF	p-value
$\chi^{t\bar{t}}$	3.6/7	0.83	4.9/7	0.67	7.4/7	0.38	4.2/7	0.76	7.7/7	0.36	5.9/7	0.55
$\Delta R_{\text{jet1}}^{\text{extra1}}$	12.1/12	0.44	6.3/12	0.90	18.9/12	0.09	46.3/12	<0.01	26.1/12	0.01	21.6/12	0.04
$\Delta R_{t,\text{close}}^{\text{extra1}}$	5.8/16	0.99	21.3/16	0.17	4.1/16	1.00	8.8/16	0.92	8.7/16	0.93	6.6/16	0.98
$\Delta R_{\text{extra1}}^{\text{extra2}}$	7.0/15	0.96	7.9/15	0.93	8.0/15	0.92	9.5/15	0.85	9.9/15	0.83	18.8/15	0.22
$\Delta R_{t,\text{close}}^{\text{extra2}}$	14.2/9	0.12	23.5/9	<0.01	10.8/9	0.29	9.6/9	0.39	7.0/9	0.63	9.4/9	0.40
$\Delta R_{\text{extra1}}^{\text{extra3}}$	2.9/6	0.82	5.0/6	0.55	2.9/6	0.83	4.2/6	0.65	3.7/6	0.72	6.9/6	0.33
$\Delta R_{t,\text{close}}^{\text{extra3}}$	7.0/7	0.42	12.1/7	0.10	5.5/7	0.59	8.9/7	0.26	10.7/7	0.15	7.3/7	0.40
$\Delta\phi^{t\bar{t}}$	4.3/6	0.63	4.2/6	0.66	11.2/6	0.08	30.5/6	<0.01	3.6/6	0.73	3.9/6	0.69
$H_{\text{T}}^{t\bar{t}}$	25.2/11	<0.01	24.8/11	<0.01	35.4/11	<0.01	27.7/11	<0.01	16.1/11	0.14	9.7/11	0.55
$R_{\text{Wb}}^{\text{leading}}$	5.0/6	0.55	3.8/6	0.71	5.4/6	0.49	3.5/6	0.74	9.0/6	0.18	6.8/6	0.34
$R_{\text{Wb}}^{\text{subleading}}$	4.6/6	0.60	3.9/6	0.69	5.6/6	0.47	2.4/6	0.88	3.2/6	0.78	4.0/6	0.67
$R_{\text{Wt}}^{\text{leading}}$	12.9/7	0.07	15.2/7	0.03	14.1/7	0.05	12.6/7	0.08	16.8/7	0.02	12.8/7	0.08
$R_{\text{Wt}}^{\text{subleading}}$	2.5/6	0.87	1.7/6	0.94	3.8/6	0.71	3.2/6	0.78	6.5/6	0.37	5.3/6	0.50
$R_{\text{jet1}}^{\text{extra1}}$	9.2/5	0.10	2.2/5	0.82	16.9/5	<0.01	43.9/5	<0.01	3.8/5	0.57	3.0/5	0.70
$R_{t,1}^{\text{extra1}}$	15.3/7	0.03	4.0/7	0.78	25.8/7	<0.01	19.8/7	<0.01	8.7/7	0.28	6.3/7	0.51
$R_{\text{extra1}}^{\text{extra2}}$	16.7/6	0.01	21.1/6	<0.01	18.4/6	<0.01	10.1/6	0.12	7.0/6	0.32	11.5/6	0.07
$R_{\text{jet1}}^{\text{extra2}}$	14.5/6	0.02	14.6/6	0.02	17.7/6	<0.01	9.2/6	0.16	5.1/6	0.53	11.2/6	0.08
$R_{t,1}^{\text{extra2}}$	6.5/5	0.26	14.0/5	0.02	5.8/5	0.33	7.2/5	0.20	10.8/5	0.06	7.8/5	0.17
$R_{\text{extra1}}^{\text{extra3}}$	13.3/5	0.02	19.7/5	<0.01	12.5/5	0.03	9.0/5	0.11	17.0/5	<0.01	14.3/5	0.01
$R_{\text{jet1}}^{\text{extra3}}$	6.9/4	0.14	8.4/4	0.08	7.3/4	0.12	7.3/4	0.12	5.7/4	0.22	7.0/4	0.13
$R_{t,1}^{\text{extra3}}$	1.6/3	0.66	2.2/3	0.54	1.9/3	0.59	3.8/3	0.29	0.4/3	0.93	2.1/3	0.55
$R_{\text{extra1}}^{t\bar{t}}$	7.7/7	0.36	9.5/7	0.22	8.5/7	0.29	8.6/7	0.28	10.5/7	0.16	12.0/7	0.10
$Z^{t\bar{t}}$	4.1/5	0.53	11.7/5	0.04	5.7/5	0.34	11.6/5	0.04	13.2/5	0.02	5.7/5	0.34
$\lvert P_{\text{cross}}^{t\bar{t}}\rvert$	4.9/10	0.90	2.7/10	0.99	7.3/10	0.70	3.0/10	0.98	2.9/10	0.98	3.5/10	0.97
$\lvert P_{\text{out}}^{t,1}\rvert$	2.7/7	0.91	28.1/7	<0.01	6.3/7	0.51	15.9/7	0.03	6.8/7	0.45	3.2/7	0.87
$\lvert y^{t,1}\rvert$	2.8/6	0.83	4.1/6	0.67	3.0/6	0.81	4.7/6	0.58	1.7/6	0.94	4.5/6	0.61
$\lvert y^{t,2}\rvert$	3.3/6	0.77	2.2/6	0.90	4.0/6	0.68	3.1/6	0.80	5.5/6	0.48	7.1/6	0.31
$\lvert y^{t\bar{t}}\rvert$	11.7/18	0.86	12.8/18	0.80	12.9/18	0.80	15.4/18	0.63	24.0/18	0.15	12.3/18	0.83
$\lvert y_{\text{boost}}^{t\bar{t}}\rvert$	11.6/15	0.71	12.1/15	0.67	12.8/15	0.62	11.2/15	0.74	16.8/15	0.33	11.8/15	0.69
N_{jets}	7.2/5	0.21	1.0/5	0.96	19.3/5	<0.01	26.1/5	<0.01	9.6/5	0.09	6.6/5	0.25
$p_{\text{T}}^{t,1}$	22.7/11	0.02	19.5/11	0.05	27.8/11	<0.01	14.9/11	0.19	29.3/11	<0.01	8.2/11	0.69
$p_{\text{T}}^{t,2}$	21.2/9	0.01	11.4/9	0.25	37.1/9	<0.01	35.6/9	<0.01	2.6/9	0.98	8.4/9	0.50
$m^{t\bar{t}}$	17.6/9	0.04	12.8/9	0.17	23.1/9	<0.01	22.3/9	<0.01	10.8/9	0.29	10.8/9	0.29
$p_{\text{T}}^{t\bar{t}}$	6.0/8	0.65	58.4/8	<0.01	7.1/8	0.52	19.3/8	0.01	27.6/8	<0.01	5.0/8	0.75

Table 8: Comparison of the measured particle-level absolute single-differential cross-sections with the predictions from several MC generators. For each prediction a χ^2 and a p-value are calculated using the covariance matrix of the measured spectrum. The number of degrees of freedom (NDF) is equal to the number of bins in the distribution.

Observable	PWG+PY8		PWG+PY8 Var. Up		PWG+PY8 Var. Down		aMC@NLO+PY8		Sherpa		PWG+H7	
	χ^2/NDF	p-value	χ^2/NDF	p-value	χ^2/NDF	p-value	χ^2/NDF	p-value	χ^2/NDF	p-value	χ^2/NDF	p-value
$\chi^{t\bar{t}}$	3.4/6	0.76	4.0/6	0.68	6.6/6	0.36	4.4/6	0.62	8.5/6	0.20	3.3/6	0.77
$\Delta R^{\text{extra1}}_{\text{jet1}}$	16.7/11	0.12	7.1/11	0.79	25.9/11	<0.01	63.7/11	<0.01	27.4/11	<0.01	17.3/11	0.10
$\Delta R^{\text{extra1}}_{t,\text{close}}$	6.9/15	0.96	21.0/15	0.14	5.8/15	0.98	13.5/15	0.57	10.8/15	0.77	10.8/15	0.77
$\Delta R^{\text{extra2}}_{\text{extra1}}$	8.4/14	0.87	8.3/14	0.88	9.3/14	0.81	10.6/14	0.72	10.5/14	0.73	26.2/14	0.02
$\Delta R^{\text{extra2}}_{t,\text{close}}$	10.4/8	0.24	13.5/8	0.10	8.8/8	0.35	6.3/8	0.61	4.7/8	0.79	4.6/8	0.80
$\Delta R^{\text{extra3}}_{\text{extra1}}$	3.2/5	0.66	3.9/5	0.56	3.1/5	0.68	5.4/5	0.37	3.5/5	0.62	8.1/5	0.15
$\Delta R^{\text{extra3}}_{t,\text{close}}$	6.9/6	0.33	7.9/6	0.25	5.9/6	0.44	12.7/6	0.05	9.9/6	0.13	8.6/6	0.20
$\Delta\phi^{t\bar{t}}$	3.9/5	0.57	2.8/5	0.74	8.3/5	0.14	31.1/5	<0.01	3.1/5	0.68	3.7/5	0.60
$H_{\text{T}}^{t\bar{t}}$	22.7/10	0.01	19.4/10	0.04	34.7/10	<0.01	34.6/10	<0.01	18.0/10	0.05	13.0/10	0.23
$R^{\text{leading}}_{\text{Wb}}$	4.8/5	0.45	2.7/5	0.74	5.4/5	0.37	2.8/5	0.73	6.5/5	0.26	4.0/5	0.55
$R^{\text{subleading}}_{\text{Wb}}$	4.8/5	0.44	4.2/5	0.52	5.1/5	0.40	2.8/5	0.73	4.1/5	0.54	2.0/5	0.85
$R^{\text{leading}}_{\text{Wt}}$	14.2/6	0.03	15.9/6	0.01	14.8/6	0.02	16.6/6	0.01	18.6/6	<0.01	15.6/6	0.02
$R^{\text{subleading}}_{\text{Wt}}$	3.2/5	0.67	2.7/5	0.75	4.0/5	0.55	4.2/5	0.52	7.6/5	0.18	3.5/5	0.62
$R^{\text{extra1}}_{\text{jet1}}$	7.7/4	0.10	2.1/4	0.72	13.6/4	<0.01	40.9/4	<0.01	3.5/4	0.47	3.0/4	0.56
$R^{\text{extra1}}_{t,1}$	13.7/6	0.03	3.0/6	0.81	22.4/6	<0.01	22.7/6	<0.01	8.5/6	0.21	7.2/6	0.30
$R^{\text{extra2}}_{\text{extra1}}$	9.5/5	0.09	10.7/5	0.06	10.2/5	0.07	12.3/5	0.03	5.8/5	0.32	6.0/5	0.30
$R^{\text{extra2}}_{\text{jet1}}$	7.5/5	0.19	6.9/5	0.23	10.2/5	0.07	3.2/5	0.67	3.4/5	0.64	4.8/5	0.44
$R^{\text{extra2}}_{t,1}$	6.7/4	0.15	12.5/4	0.01	6.2/4	0.19	6.6/4	0.16	10.4/4	0.03	8.1/4	0.09
$R^{\text{extra3}}_{\text{extra1}}$	11.0/4	0.03	14.1/4	<0.01	10.1/4	0.04	6.3/4	0.18	14.9/4	<0.01	13.5/4	<0.01
$R^{\text{extra3}}_{\text{jet1}}$	6.8/3	0.08	7.4/3	0.06	7.2/3	0.07	7.0/3	0.07	5.3/3	0.15	7.2/3	0.07
$R^{\text{extra3}}_{t,1}$	1.0/2	0.62	1.4/2	0.49	0.9/2	0.63	1.4/2	0.49	0.3/2	0.86	0.8/2	0.66
$R^{\text{t}\bar{\text{t}}}_{\text{extra1}}$	6.5/6	0.37	9.7/6	0.14	5.9/6	0.43	9.9/6	0.13	14.4/6	0.03	18.0/6	<0.01
$Z^{t\bar{t}}$	3.8/4	0.43	11.6/4	0.02	4.9/4	0.30	23.3/4	<0.01	12.5/4	0.01	4.4/4	0.35
$\lvert P^{t\bar{t}}_{\text{cross}}\rvert$	6.1/9	0.73	3.0/9	0.96	8.3/9	0.50	4.9/9	0.84	1.7/9	1.00	2.6/9	0.98
$\lvert P^{t,1}_{\text{out}}\rvert$	3.3/6	0.77	6.2/6	0.41	7.5/6	0.28	12.3/6	0.05	1.1/6	0.98	2.6/6	0.86
$\lvert y^{t,1}\rvert$	1.1/5	0.96	2.1/5	0.83	0.9/5	0.97	2.0/5	0.85	0.9/5	0.97	2.0/5	0.85
$\lvert y^{t,2}\rvert$	3.8/5	0.57	1.6/5	0.90	4.9/5	0.42	3.1/5	0.68	5.8/5	0.32	4.9/5	0.43
$\lvert y^{t\bar{t}}\rvert$	12.0/17	0.80	13.2/17	0.72	12.7/17	0.76	16.2/17	0.51	22.1/17	0.18	11.8/17	0.81
$\lvert y^{t\bar{t}}_{\text{boost}}\rvert$	10.1/14	0.76	11.6/14	0.64	9.9/14	0.77	12.8/14	0.54	15.3/14	0.36	11.4/14	0.65
N_{jets}	5.0/4	0.29	0.8/4	0.94	13.7/4	<0.01	27.8/4	<0.01	6.4/4	0.17	1.5/4	0.82
$p_{\text{T}}^{t,1}$	15.3/10	0.12	11.6/10	0.31	21.2/10	0.02	12.7/10	0.24	30.6/10	<0.01	8.7/10	0.56
$p_{\text{T}}^{t,2}$	19.1/8	0.01	9.3/8	0.32	37.7/8	<0.01	45.3/8	<0.01	3.4/8	0.91	10.3/8	0.24
$m^{t\bar{t}}$	19.9/8	0.01	12.8/8	0.12	26.9/8	<0.01	26.5/8	<0.01	9.8/8	0.28	10.3/8	0.24
$p_{\text{T}}^{t\bar{t}}$	4.4/7	0.73	18.1/7	0.01	10.2/7	0.18	15.6/7	0.03	13.2/7	0.07	6.3/7	0.50

Table 9: Comparison of the measured particle-level normalised single-differential cross-sections with the predictions from several MC generators. For each prediction a χ^2 and a p-value are calculated using the covariance matrix of the measured spectrum. The number of degrees of freedom (NDF) is equal to the number of bins in the distribution minus one.

Observable	PWG+PY8		PWG+PY8 Var. Up		PWG+PY8 Var. Down		aMC@NLO+PY8		Sherpa		PWG+H7	
	χ^2/NDF	p-value	χ^2/NDF	p-value	χ^2/NDF	p-value	χ^2/NDF	p-value	χ^2/NDF	p-value	χ^2/NDF	p-value
$\lvert P^{t\bar{t}}_{\text{cross}}\rvert$ vs N_{jets}	20.5/13	0.08	5.9/13	0.95	43.7/13	<0.01	44.2/13	<0.01	23.7/13	0.03	9.8/13	0.71
$\lvert P^{t,1}_{\text{out}}\rvert$ vs N_{jets}	49.8/14	<0.01	50.3/14	<0.01	79.9/14	<0.01	90.6/14	<0.01	38.6/14	<0.01	17.4/14	0.23
$p_{\text{T}}^{t,1}$ vs N_{jets}	29.3/19	0.06	20.6/19	0.36	48.3/19	<0.01	62.1/19	<0.01	38.1/19	<0.01	22.9/19	0.24
$p_{\text{T}}^{t,1}$ vs $m^{t\bar{t}}$	27.8/11	<0.01	19.2/11	0.06	39.3/11	<0.01	37.4/11	<0.01	13.8/11	0.24	13.8/11	0.24
$p_{\text{T}}^{t,1}$ vs $p_{\text{T}}^{t,2}$	22.8/12	0.03	25.8/12	0.01	33.7/12	<0.01	33.7/12	<0.01	29.7/12	<0.01	7.3/12	0.83
$p_{\text{T}}^{t,2}$ vs N_{jets}	26.9/14	0.02	22.3/14	0.07	46.2/14	<0.01	91.1/14	<0.01	30.1/14	<0.01	31.8/14	<0.01
$p_{\text{T}}^{t,2}$ vs $m^{t\bar{t}}$	15.9/12	0.20	7.5/12	0.82	32.5/12	<0.01	26.6/12	<0.01	10.9/12	0.53	8.4/12	0.75
$p_{\text{T}}^{t\bar{t}}$ vs N_{jets}	34.6/11	<0.01	52.1/11	<0.01	59.7/11	<0.01	135.0/11	<0.01	33.3/11	<0.01	18.0/11	0.08
$p_{\text{T}}^{t\bar{t}}$ vs $m^{t\bar{t}}$	35.8/11	<0.01	92.8/11	<0.01	35.9/11	<0.01	33.3/11	<0.01	46.4/11	<0.01	17.3/11	0.10

Table 10: Comparison of the measured particle-level absolute double-differential cross-sections with the predictions from several MC generators. For each prediction a χ^2 and a p-value are calculated using the covariance matrix of the measured spectrum. The number of degrees of freedom (NDF) is equal to the number of bins in the distribution.

Observable	PWG+PY8		PWG+PY8 Var. Up		PWG+PY8 Var. Down		aMC@NLO+PY8		Sherpa		PWG+H7	
	χ^2/NDF	p-value	χ^2/NDF	p-value	χ^2/NDF	p-value	χ^2/NDF	p-value	χ^2/NDF	p-value	χ^2/NDF	p-value
$\lvert P^{t\bar{t}}_{\text{cross}}\rvert$ vs N_{jets}	14.3/12	0.28	5.8/12	0.93	30.6/12	<0.01	50.1/12	<0.01	16.7/12	0.16	8.2/12	0.77
$\lvert P^{t,1}_{\text{out}}\rvert$ vs N_{jets}	53.4/13	<0.01	35.4/13	<0.01	85.2/13	<0.01	111.0/13	<0.01	28.4/13	<0.01	26.3/13	0.02
$p_{\text{T}}^{t,1}$ vs N_{jets}	22.6/18	0.21	22.0/18	0.23	34.2/18	0.01	65.0/18	<0.01	40.2/18	<0.01	24.9/18	0.13
$p_{\text{T}}^{t,1}$ vs $m^{t\bar{t}}$	31.9/10	<0.01	17.0/10	0.08	48.1/10	<0.01	46.8/10	<0.01	11.3/10	0.34	15.5/10	0.11
$p_{\text{T}}^{t,1}$ vs $p_{\text{T}}^{t,2}$	16.6/11	0.12	21.5/11	0.03	25.4/11	<0.01	36.7/11	<0.01	28.9/11	<0.01	10.2/11	0.51
$p_{\text{T}}^{t,2}$ vs N_{jets}	25.9/13	0.02	14.6/13	0.34	49.1/13	<0.01	113.0/13	<0.01	18.6/13	0.14	23.4/13	0.04
$p_{\text{T}}^{t,2}$ vs $m^{t\bar{t}}$	21.1/11	0.03	6.3/11	0.85	39.8/11	<0.01	36.0/11	<0.01	8.9/11	0.64	8.3/11	0.69
$p_{\text{T}}^{t\bar{t}}$ vs N_{jets}	28.9/10	<0.01	16.7/10	0.08	56.0/10	<0.01	144.0/10	<0.01	21.7/10	0.02	12.0/10	0.29
$p_{\text{T}}^{t\bar{t}}$ vs $m^{t\bar{t}}$	50.6/10	<0.01	103.0/10	<0.01	52.9/10	<0.01	42.4/10	<0.01	62.2/10	<0.01	28.1/10	<0.01

Table 11: Comparison of the measured particle-level normalised double-differential cross-sections with the predictions from several MC generators. For each prediction a χ^2 and a p-value are calculated using the covariance matrix of the measured spectrum. The number of degrees of freedom (NDF) is equal to the number of bins in the distribution minus one.

10.1.2 Cross-sections in the full phase space

Tables 12 and 13 show the quantitative comparisons among the single-differential parton-level results and theoretical predictions, while Tables 14 and 15 show the results of the double-differential cross-sections. Similar conclusions can be drawn as for the χ^2 of the particle-level measurements, although a few minor differences can be seen. For example, the absolute differential cross-section as a function of the $H_{\mathrm{T}}^{t\bar{t}}$ variable has slightly larger p-values when unfolded to the full phase space; the same conclusion cannot be drawn when comparing the normalised differential cross-section as a function of the $H_{\mathrm{T}}^{t\bar{t}}$. Conversely, the differential cross-section as a function of $\Delta\phi^{t\bar{t}}$ has smaller p-values but remains in good agreement with the data. Once more, Powheg+Herwig7 and Powheg+Pythia8 perform best in terms of reproducing the data, while MadGraph5_aMC@NLO+Pythia8 typically fails to reflect the data. The Sherpa predictions disagree more with the parton-level measurements compared to their performance at particle level; this conclusion is valid with the exception of single-differential absolute cross sections where most of the p-values are acceptable.

Observable	PWG+PY8		PWG+PY8 Var. Up		PWG+PY8 Var. Down		aMC@NLO+PY8		Sherpa		PWG+H7	
	χ^2/NDF	p-value	χ^2/NDF	p-value	χ^2/NDF	p-value	χ^2/NDF	p-value	χ^2/NDF	p-value	χ^2/NDF	p-value
$\chi^{t\bar{t}}$	2.7/7	0.91	2.6/7	0.92	3.6/7	0.82	4.1/7	0.76	2.1/7	0.95	2.5/7	0.93
$\Delta\phi$	3.3/6	0.77	2.7/6	0.85	4.7/6	0.59	17.1/6	<0.01	9.6/6	0.14	4.8/6	0.58
$H_{\mathrm{T}}^{t\bar{t}}$	14.9/11	0.19	13.0/11	0.29	20.4/11	0.04	14.8/11	0.19	20.7/11	0.04	11.8/11	0.38
$\lvert y^{t,1}\rvert$	1.7/7	0.97	1.7/7	0.97	1.8/7	0.97	1.6/7	0.98	1.6/7	0.98	1.5/7	0.98
$\lvert y^{t,2}\rvert$	2.3/6	0.89	2.3/6	0.89	2.4/6	0.89	2.3/6	0.89	2.5/6	0.87	2.3/6	0.89
$\lvert y^{t\bar{t}}\rvert$	6.9/12	0.86	6.7/12	0.88	6.9/12	0.86	6.9/12	0.86	7.5/12	0.82	6.8/12	0.87
$\lvert y^{t\bar{t}}_{\mathrm{boost}}\rvert$	11.4/15	0.72	11.1/15	0.75	11.5/15	0.72	11.3/15	0.73	12.3/15	0.65	11.3/15	0.73
$p_{\mathrm{T}}^{t,1}$	17.7/10	0.06	23.0/10	0.01	18.2/10	0.05	11.5/10	0.32	30.3/10	<0.01	13.5/10	0.20
$p_{\mathrm{T}}^{t,2}$	4.6/8	0.80	2.6/8	0.96	8.6/8	0.38	5.4/8	0.71	7.1/8	0.53	3.3/8	0.92
$m^{t\bar{t}}$	17.4/9	0.04	19.1/9	0.02	16.1/9	0.06	17.1/9	0.05	19.7/9	0.02	17.2/9	0.05
$p_{\mathrm{T}}^{t\bar{t}}$	4.3/5	0.50	35.3/5	<0.01	3.1/5	0.68	36.3/5	<0.01	21.5/5	<0.01	4.4/5	0.49

Table 12: Comparison of the measured parton-level absolute single-differential cross-sections with the predictions from several MC generators. For each prediction a χ^2 and a p-value are calculated using the covariance matrix of the measured spectrum. The number of degrees of freedom (NDF) is equal to the number of bins in the distribution.

Observable	PWG+PY8		PWG+PY8 Var. Up		PWG+PY8 Var. Down		aMC@NLO+PY8		Sherpa		PWG+H7	
	χ^2/NDF	p-value	χ^2/NDF	p-value	χ^2/NDF	p-value	χ^2/NDF	p-value	χ^2/NDF	p-value	χ^2/NDF	p-value
$\chi^{t\bar{t}}$	3.6/6	0.73	2.8/6	0.84	5.3/6	0.50	4.3/6	0.63	3.4/6	0.75	3.0/6	0.81
$\Delta\phi$	3.6/5	0.60	2.5/5	0.77	5.2/5	0.40	17.7/5	<0.01	10.1/5	0.07	5.8/5	0.33
$H_{\mathrm{T}}^{t\bar{t}}$	31.3/10	<0.01	25.1/10	<0.01	40.3/10	<0.01	32.1/10	<0.01	42.7/10	<0.01	24.3/10	<0.01
$\lvert y^{t,1}\rvert$	1.8/6	0.94	1.8/6	0.94	1.9/6	0.93	1.7/6	0.95	1.7/6	0.95	1.6/6	0.95
$\lvert y^{t,2}\rvert$	3.6/5	0.61	3.4/5	0.64	3.8/5	0.58	3.2/5	0.66	3.8/5	0.57	3.6/5	0.61
$\lvert y^{t\bar{t}}\rvert$	6.8/11	0.82	6.5/11	0.83	6.8/11	0.81	6.7/11	0.83	7.5/11	0.76	6.7/11	0.82
$\lvert y^{t\bar{t}}_{\mathrm{boost}}\rvert$	11.1/14	0.68	10.8/14	0.70	11.1/14	0.68	11.1/14	0.68	12.0/14	0.60	11.0/14	0.69
$p_{\mathrm{T}}^{t,1}$	25.9/9	<0.01	29.5/9	<0.01	27.6/9	<0.01	17.3/9	0.04	46.5/9	<0.01	19.4/9	0.02
$p_{\mathrm{T}}^{t,2}$	14.7/7	0.04	6.6/7	0.47	25.2/7	<0.01	17.8/7	0.01	16.4/7	0.02	9.7/7	0.21
$m^{t\bar{t}}$	32.7/8	<0.01	35.6/8	<0.01	29.7/8	<0.01	35.9/8	<0.01	39.2/8	<0.01	33.1/8	<0.01
$p_{\mathrm{T}}^{t\bar{t}}$	6.1/4	0.19	36.9/4	<0.01	6.2/4	0.18	44.7/4	<0.01	21.9/4	<0.01	9.3/4	0.05

Table 13: Comparison of the measured parton-level normalised single-differential cross-sections with the predictions from several MC generators. For each prediction a χ^2 and a p-value are calculated using the covariance matrix of the measured spectrum. The number of degrees of freedom (NDF) is equal to the number of bins in the distribution minus one.

Observable	PWG+PY8		PWG+PY8 Var. Up		PWG+PY8 Var. Down		aMC@NLO+PY8		Sherpa		PWG+H7	
	χ^2/NDF	p-value	χ^2/NDF	p-value	χ^2/NDF	p-value	χ^2/NDF	p-value	χ^2/NDF	p-value	χ^2/NDF	p-value
$p_{\mathrm{T}}^{t,1}$ vs $m^{t\bar{t}}$	17.9/10	0.06	20.5/10	0.02	23.3/10	<0.01	31.1/10	<0.01	26.7/10	<0.01	14.4/10	0.15
$p_{\mathrm{T}}^{t,1}$ vs $p_{\mathrm{T}}^{t,2}$	22.4/12	0.03	37.2/12	<0.01	25.7/12	0.01	32.0/12	<0.01	45.6/12	<0.01	16.8/12	0.16
$p_{\mathrm{T}}^{t,2}$ vs $m^{t\bar{t}}$	13.5/13	0.41	16.1/13	0.25	16.8/13	0.21	15.6/13	0.27	19.6/13	0.10	13.1/13	0.44
$p_{\mathrm{T}}^{t\bar{t}}$ vs $m^{t\bar{t}}$	21.4/12	0.04	56.0/12	<0.01	19.4/12	0.08	52.4/12	<0.01	37.5/12	<0.01	18.0/12	0.12

Table 14: Comparison of the measured parton-level absolute double-differential cross-sections with the predictions from several MC generators. For each prediction a χ^2 and a p-value are calculated using the covariance matrix of the measured spectrum. The number of degrees of freedom (NDF) is equal to the number of bins in the distribution.

Observable	PWG+PY8		PWG+PY8 Var. Up		PWG+PY8 Var. Down		aMC@NLO+PY8		Sherpa		PWG+H7	
	χ^2/NDF	p-value	χ^2/NDF	p-value	χ^2/NDF	p-value	χ^2/NDF	p-value	χ^2/NDF	p-value	χ^2/NDF	p-value
$p_{\mathrm{T}}^{t,1}$ vs $m^{t\bar{t}}$	39.2/9	<0.01	30.4/9	<0.01	53.5/9	<0.01	66.9/9	<0.01	49.2/9	<0.01	33.3/9	<0.01
$p_{\mathrm{T}}^{t,1}$ vs $p_{\mathrm{T}}^{t,2}$	33.4/11	<0.01	39.9/11	<0.01	45.6/11	<0.01	65.3/11	<0.01	58.4/11	<0.01	27.1/11	<0.01
$p_{\mathrm{T}}^{t,2}$ vs $m^{t\bar{t}}$	21.4/12	0.04	17.3/12	0.14	31.5/12	<0.01	31.2/12	<0.01	28.1/12	<0.01	18.2/12	0.11
$p_{\mathrm{T}}^{t\bar{t}}$ vs $m^{t\bar{t}}$	39.6/11	<0.01	68.7/11	<0.01	38.8/11	<0.01	105.0/11	<0.01	53.1/11	<0.01	42.7/11	<0.01

Table 15: Comparison of the measured parton-level normalised double-differential cross-sections with the predictions from several MC generators. For each prediction a χ^2 and a p-value are calculated using the covariance matrix of the measured spectrum. The number of degrees of freedom (NDF) is equal to the number of bins in the distribution minus one.

10.2 Discussion of individual observables

In the following Sections, trends in specific observables are discussed. In particular, in the Section 10.2.1, particle-level results are shown for selected normalised single-differential cross-sections. Similarly, selected parton-level results, are discussed in the Section 10.2.2.

While a large variety of observables has been considered in this analysis, as presented in Section 7, the present section focuses on selected variables either to illustrate features when data is compared to predictions or to achieve a comparison with other measurements done by the ATLAS experiment, in the ℓ+jets channel of the top-quark pair [3].

10.2.1 Results at particle level

Single-differential cross-sections are presented in Figures 5–14 for selected observables. These observables fall into two categories:

- characteristic kinematic variables of the top-quark candidates or the top-quark pair system, specifically the transverse momentum of the leading and sub-leading top-quark candidates, the top-quark pair p_{T} and mass, the azimuthal angle between the two top-quark candidates ($\Delta\phi^{t\bar{t}}$), the p_{T} ratio of the daughter W boson of the leading top-quark candidate to its parent ($R_{Wt}^{\mathrm{leading}}$);
- variables that compare the identified 'extra jets' to the $t\bar{t}$ system kinematic properties, such as the ratio of the leading 'extra jet' p_{T} to the top-quark p_{T} and of the sub-leading 'extra jet' p_{T} to the leading 'extra jet' p_{T}, as well as the ΔR between the leading 'extra jet' and the leading jet. These observables explicitly differentiate between jets from the top-quark pair system and additional radiation.

Figure 5 shows the measured normalised differential cross-sections as a function of the leading and sub-leading top-quark transverse momenta. For illustration, these are shown alongside the detector-level distributions. The detector-level distributions indicate that a good signal purity is achieved, with *e.g.* a background contamination of 30% or less for $p_{\mathrm{T}}^{t,1} > 200$ GeV. The breakdown of the systematic uncertainties is shown on Figure 6. The less collimated top-quark decays at low top-quark transverse momenta lead to a smaller signal-background separation, which in the case of the sub-leading top-quark p_{T} distribution causes the background uncertainty to be dominant, whereas the radiation and PDF uncertainties are most important at large p_{T}. In the case of the leading top-quark p_{T}, the dominant uncertainties are from theoretical sources at low p_{T}, mainly from the matrix element calculation, while at high p_{T} no individual uncertainty source dominates.

Similar trends are seen in both observables, showing that the event generators predict a harder p_{T} spectrum than what is observed in data. These slopes are mostly significant with respect to the uncertainties. The data are mostly consistent with the predictions from Sherpa, Powheg+Herwig7 and Powheg+Pythia8 with increased radiation.

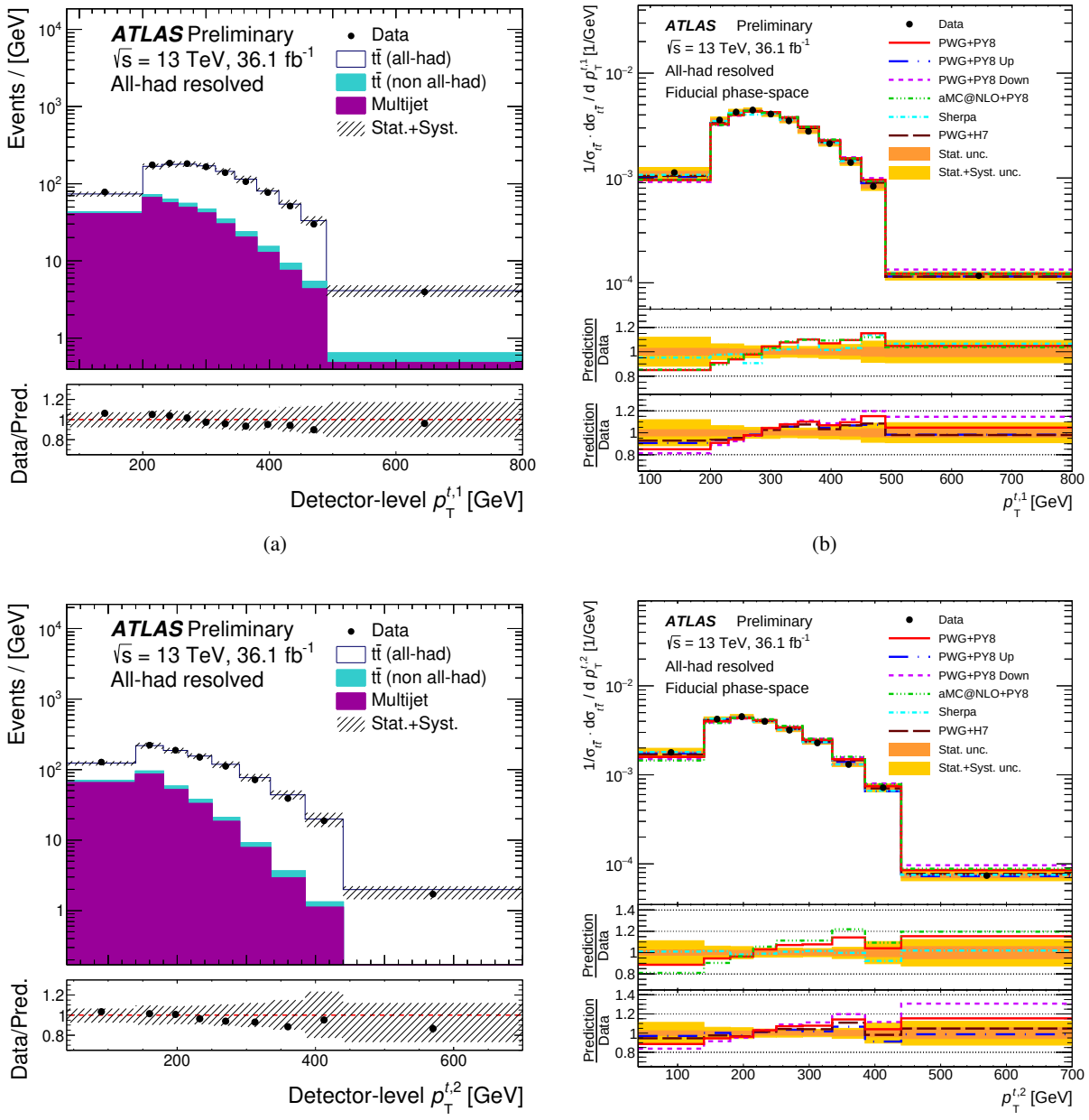

(a) (b)

(c) (d)

Figure 5: Comparison of the ATLAS data to the fully simulated nominal SM predictions for the (a) leading and (c) sub-leading top-quark transverse momenta. The shaded bands represent the uncertainties on the total prediction. Data points are placed at the centre of each bin. The lower panel shows the ratios of the theoretical predictions to data. Single-differential normalised cross-section measurements, unfolded at particle level, as a function of the (b) leading and (d) sub-leading top-quark transverse momenta. The unfolded data are compared to theoretical predictions. In the top panel, the unfolded data are shown as black points, while lines indicate the predictions from several MC programmes. Uncertainties are shown by the shaded bands. The lower two panels show the ratio of the MC predictions to the unfolded data.

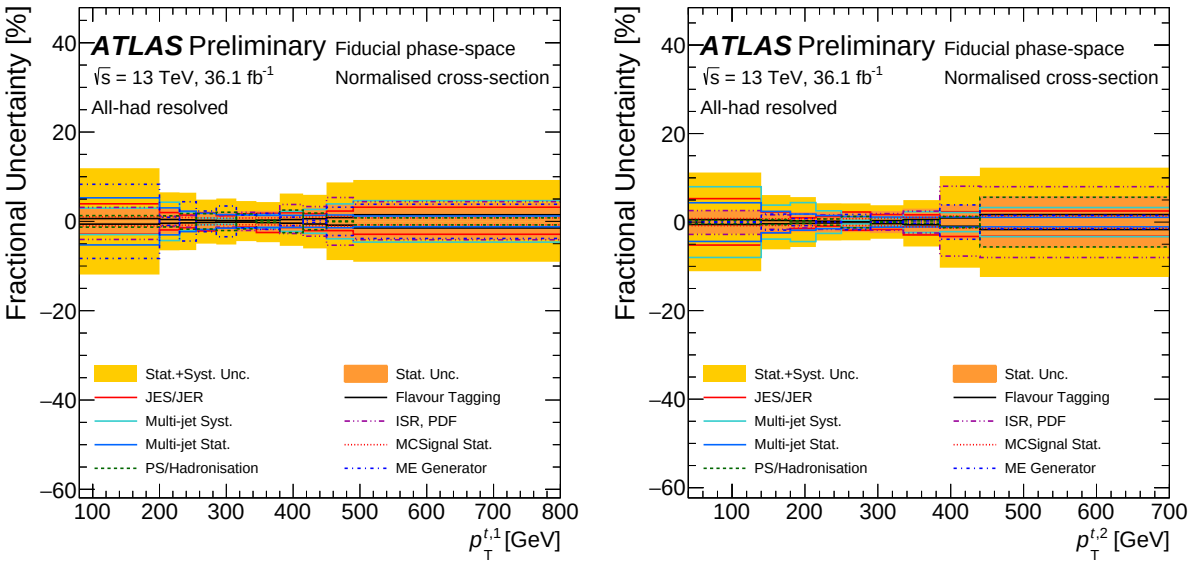

(a) (b)

Figure 6: Fractional uncertainties for the normalised single-differential distributions unfolded at particle level as a function of the (a) leading and (b) sub-leading top-quark transverse momenta. The bands represent the uncertainties on the unfolded data. Lines indicate the breakdown of the major components of the uncertainties.

The particle-level absolute differential cross-section measurement for the leading top-quark p_{T} is shown in Figure 7, for comparison with the normalised measurement shown in Figure 5(b). It can clearly be seen that the normalisation substantially reduces the total uncertainties, particularly those originating from the parton shower and hadronisation, improving sensitivity to mismodelling of the distributions.

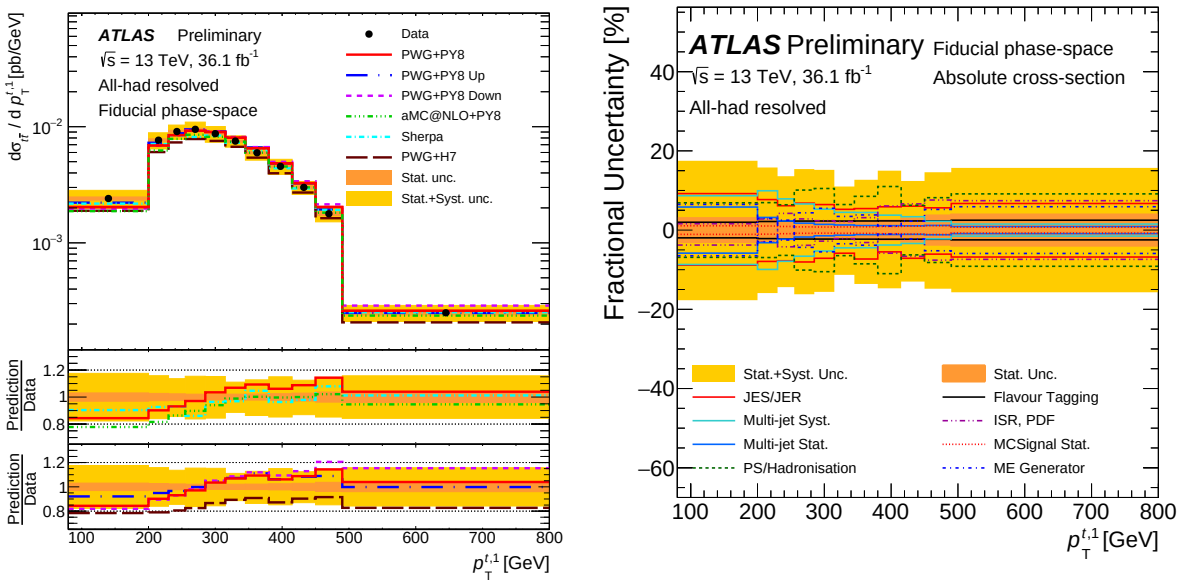

(a) (b)

Figure 7: Particle-level single-differential absolute cross-section measurement (a), as a function of the leading top-quark transverse momentum. The unfolded data are compared to theoretical predictions. In the top panel, the unfolded data are shown as black points, while lines indicate the predictions from several MC programmes. Uncertainties are shown by the shaded bands. The lower two panels show the ratio of the MC predictions to the unfolded data. Fractional uncertainties (b) for the absolute single-differential cross-sections as a function of the leading top-quark transverse momentum. The bands represent the uncertainties on the unfolded data. Lines indicate the breakdown of the major components of the uncertainties.

Two features of the $t\bar{t}$ system are shown in Figure 8, namely the top-quark pair transverse momentum and the top-quark pair mass. The $p_{\mathrm{T}}^{t\bar{t}}$ distribution mostly agrees well with the nominal Powheg+Pythia8 prediction, but substantial deviations are seen with respect to the MadGraph5_aMC@NLO+Pythia8 and Sherpa predictions, which predict spectra that are respectively too soft and too hard at high $p_{\mathrm{T}}^{t\bar{t}}$. The Powheg+Pythia8 `Var3cUp` variation is also harder than the data, which is at odds with the observations on the top-quark transverse momenta in Figure 5, where this generator reproduces the data better than the nominal Powheg+Pythia8 configuration. On the other hand, the $m^{t\bar{t}}$ distribution shows the same features as already observed in the individual top-quark p_{T} distributions, since for central top-quark production the mass is dominated by the top-quark transverse momenta.

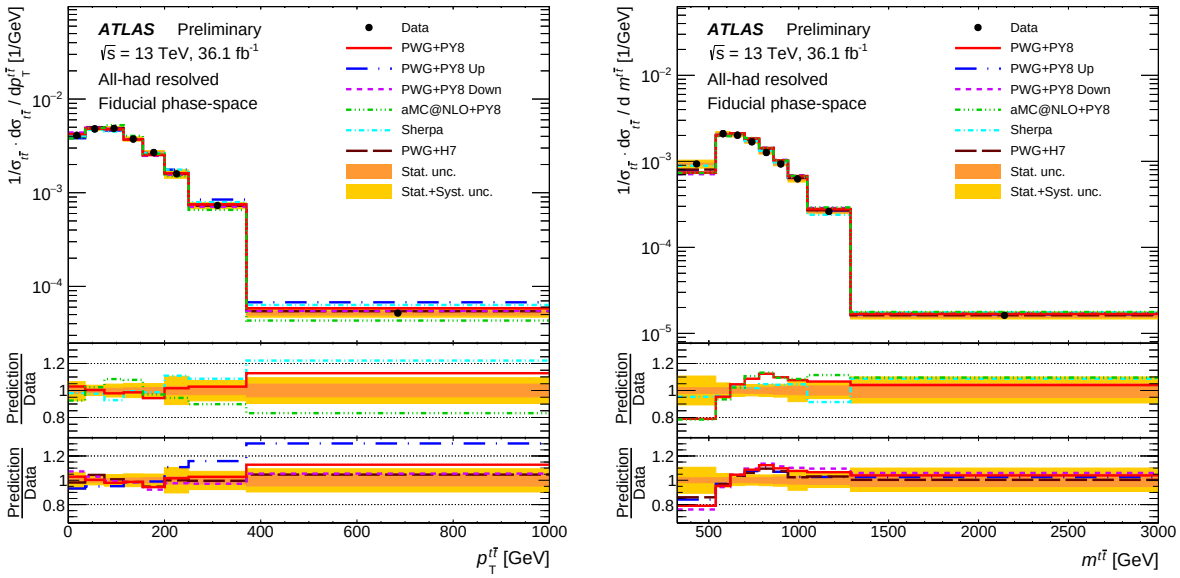

(a) (b)

Figure 8: Particle-level normalised single-differential cross-sections as a function of the (a) transverse momentum of $t\bar{t}$ system and of the (b) $t\bar{t}$ system mass, compared with different MC predictions. In the top panel, the unfolded data are shown as black points, while lines indicate the predictions from several MC programmes. Uncertainties are shown by the shaded bands. The lower two panels show the ratio of the MC predictions to the unfolded data.

Given that in the all-hadronic channel the four-momenta of both top quarks are fully reconstructed, angular distributions are important observables to study in this channel. One such observable is the azimuthal separation between the top quarks, $\Delta\phi^{t\bar{t}}$, as shown in Figure 9, which may be sensitive to BSM couplings, and is influenced by the $p_{\mathrm{T}}^{t\bar{t}}$ distribution. Deviations from the data are observed for both POWHEG+PYTHIA8 alternative samples and for MADGRAPH5_aMC@NLO+PYTHIA8, but for the nominal POWHEG+PYTHIA8 configuration good agreement is observed.

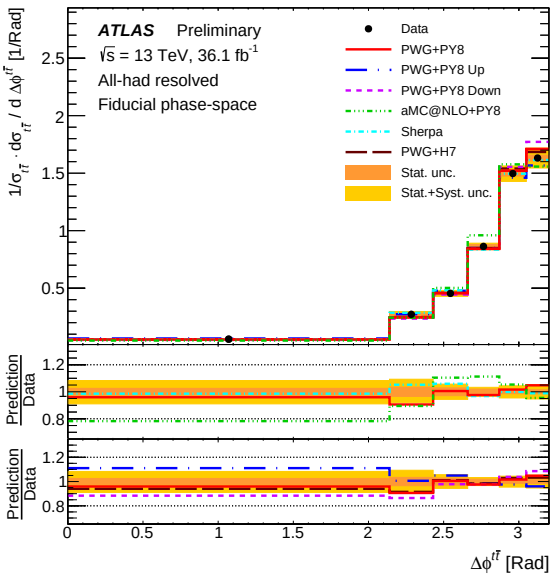

Figure 9: Particle-level normalised single-differential cross-sections as a function of the azimuthal separation $\Delta\phi^{t\bar{t}}$ between the two top-quark candidates. In the top panel, the unfolded data are shown as black points, while lines indicate the predictions from several MC programmes. Uncertainties are shown by the shaded bands. The lower two panels show the ratio of the MC predictions to the unfolded data.

Kinematic correlations in the top-quark decay process are probed, for example, by the ratio of the p_{T} of the W boson and the top quark. For the leading top quark, this distribution is shown in Figure 10. All MC predictions show poor agreement for this observable, with p-values at or below the 10% level. The data favours a slightly higher proportion of events where this ratio is extremal, closer to 0 or to 1.

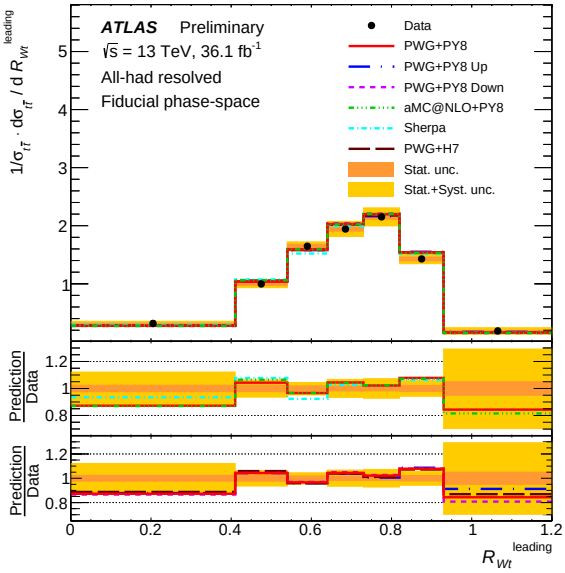

Figure 10: Particle-level normalised single-differential cross-section as a function of the ratio of W-boson p_{T} to parent top-quark p_{T} for the leading top quark, $R_{Wt}^{\mathrm{leading}}$. In the top panel, the unfolded data are shown as black points, while lines indicate the predictions from several MC programmes. Uncertainties are shown by the shaded bands. The lower two panels show the ratio of the MC predictions to the unfolded data.

One of the chief goals of this paper is to characterise the modelling of jet radiation accompanying $t\bar{t}$ production. The unfolded jet multiplicity distribution is shown in Figure 11. From Figure 2, the signal purity is seen to be relatively good for $N_{\mathrm{jets}} < 10$, and the background uncertainties on the normalised cross-section (Figure 11(b)) are small compared to theoretical uncertainties. Thus, conclusions can be safely drawn about the properties of up to three emissions, which will be discussed subsequently.

Matrix element, ISR and parton shower/hadronisation uncertainties are dominant in most jet multiplicity bins, while jet energy scale and resolution uncertainties are large both for the 7-jet bin and for events with at least 10 jets. The data favour more radiation than is produced by the nominal Powheg+Pythia8 configuration, being more consistent with the `Var3cUp` variation as well as with Powheg+Herwig7. While Sherpa and MadGraph5_aMC@NLO+Pythia8 also reproduce the data fairly well, but disagree on the frequency of a single hard emission.

Figure 12 shows the differential cross-section as a function of two p_{T} ratios computed with the jets originating outside the $t\bar{t}$ decay. The p_{T} of the first ISR emission and the leading top-quark p_{T} are both important scales for the $t\bar{t}$ production process. This ratio $R_{t,1}^{\mathrm{extra1}}$ compares these two scales and shows a significant departure from the data for a number of generators. Systematic uncertainties on the background estimation are dominant for the $R_{t,1}^{\mathrm{extra1}}$ distribution, but are substantially smaller than the observed deviation. The background uncertainty is comparable to the modelling uncertainties for $R_{t,1}^{\mathrm{extra2}}$, but is also dominant for $R_{t,1}^{\mathrm{extra3}}$. It is observed that the leading extra jet p_{T} spectrum has a mode at around a quarter of the leading top-quark p_{T}, and exceeds the leading top-quark p_{T} at a low rate. Consistent with other observations,

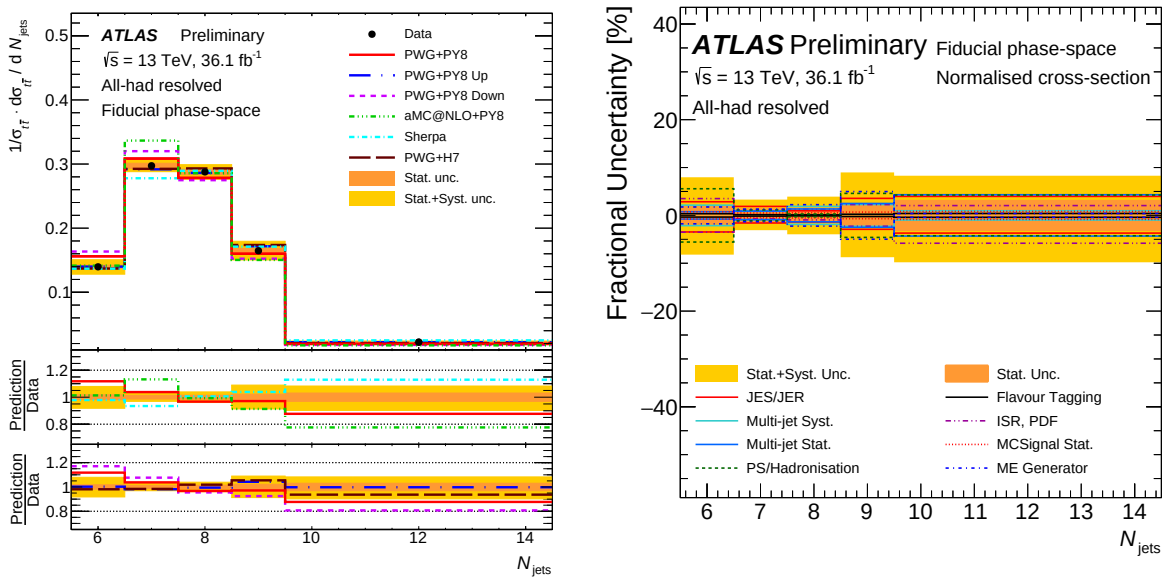

(a) (b)

Figure 11: Single-differential normalised cross-section measurements (a), unfolded at particle level, as a function of the jet multiplicity. In the top panel, the unfolded data are shown as black points, while lines indicate the predictions from several MC programmes. Uncertainties are shown by the shaded bands. The lower two panels show the ratio of the MC predictions to the unfolded data. Fractional uncertainties (b) for the normalised single-differential distributions unfolded at particle level as a function of the jet multiplicity. The bands represent the uncertainties on the unfolded data. Lines indicate the breakdown of the major components of the uncertainties.

the nominal POWHEG+PYTHIA8 configuration produces a first emission that is too soft with respect to the data, as does MADGRAPH5_aMC@NLO+PYTHIA8. The second emission p_{T} peaks slightly lower than the first. While reproduced better than the leading emission, all simulations produce too many events with $R_{t,1}^{\mathrm{extra2}}$close to 0.3, and too few elsewhere. The third emission p_{T} does not show significant deviations from the data.

In events with substantial ISR, the leading extra jet may provide the relevant scale for the process. The distribution of $R_{\mathrm{extra1}}^{\mathrm{extra2}}$(Figure 13) tests the second emission modelling relative to the leading extra jet p_{T}, and shows a minor trend. Cancellation of systematic uncertainties, notably those on the background prediction, across the spectrum results in small uncertainties on the $R_{\mathrm{extra1}}^{\mathrm{extra2}}$distribution in all bins. The sub-leading extra jet p_{T} is broadly peaked just below half the leading extra jet p_{T}, with a skew towards higher values.

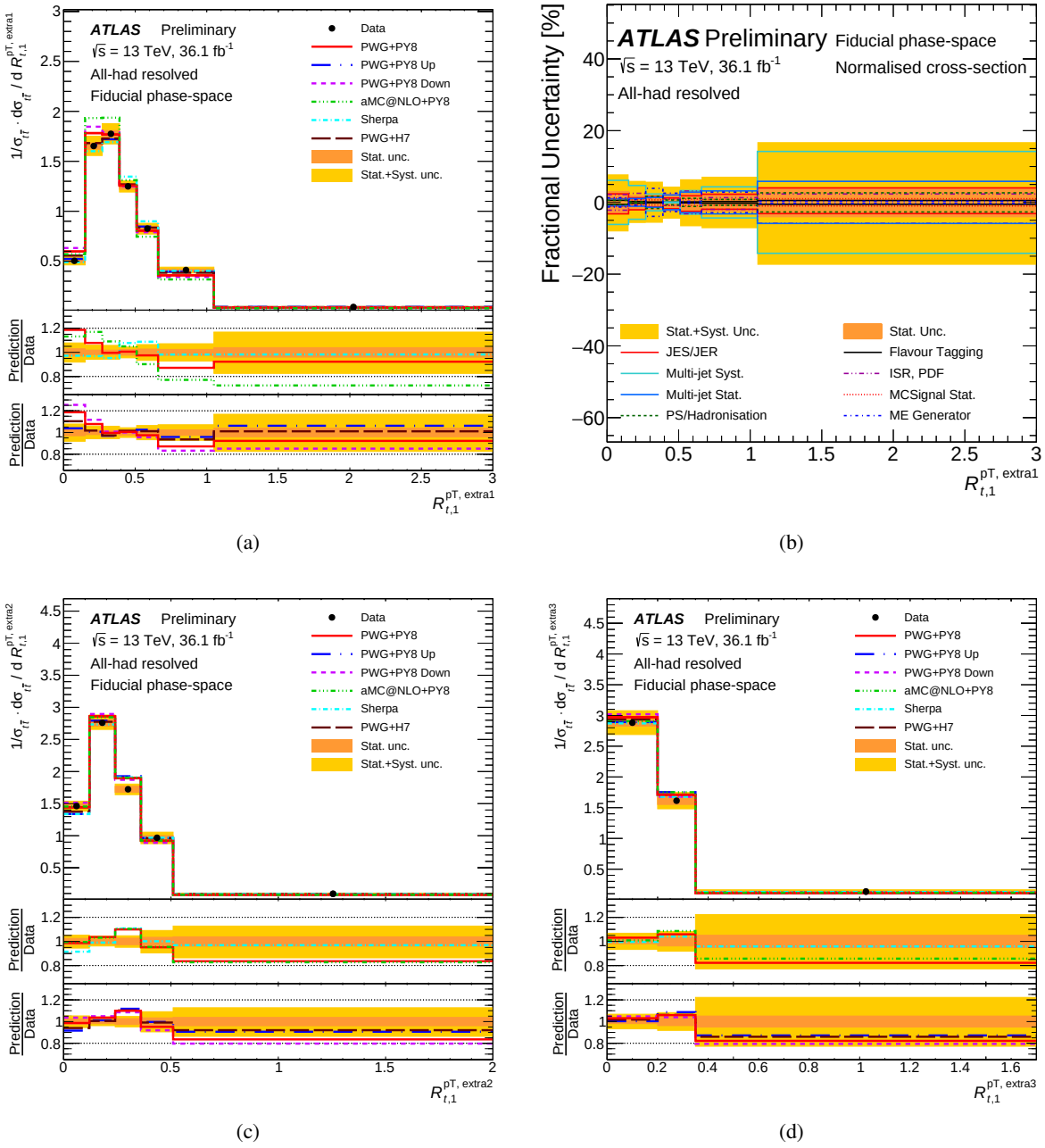

Figure 12: Particle-level single differential normalised cross sections (a,c,d) as a function of the ratio of the leading (a), sub-leading (c) and sub-subleading (d) 'extra jet' p_{T} to the leading top-quark p_{T}. In the top panel, the unfolded data are shown as black points, while lines indicate the predictions from several MC programmes. Uncertainties are shown by the shaded bands. The lower two panels show the ratio of the MC predictions to the unfolded data. Fractional uncertainties (b) for the normalised single-differential cross-sections as a function of the ratio of leading 'extra jet' p_{T} to the leading top-quark p_{T}. The bands represent the uncertainties on the unfolded data. Lines indicate the breakdown of the major components of the uncertainties.

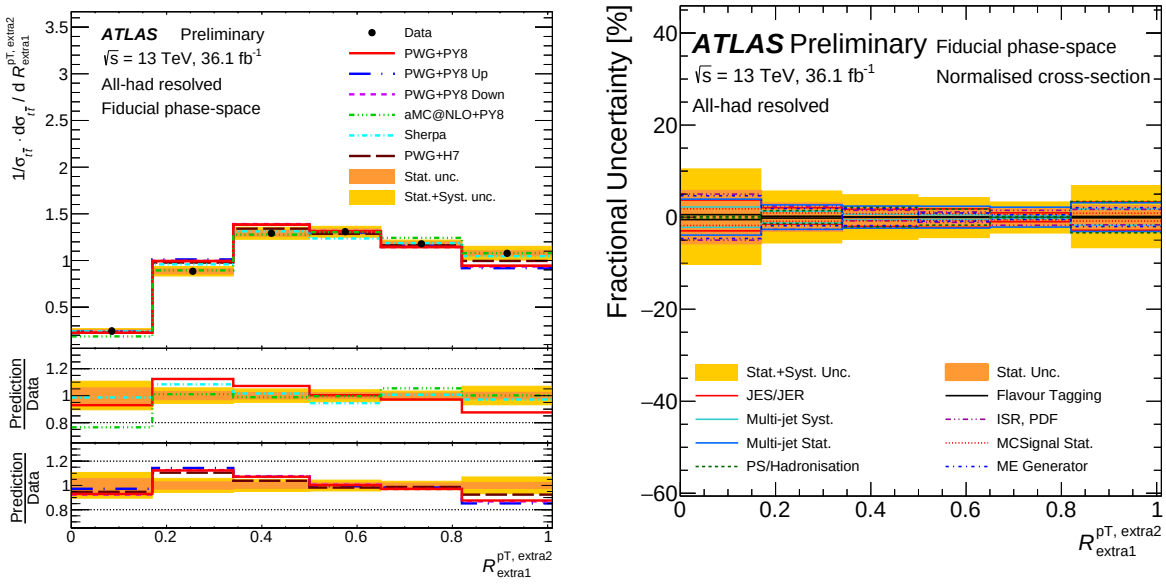

(a) (b)

Figure 13: Particle-level single differential normalised cross sections (a) as a function of the ratio of sub-leading 'extra jet' p_{T} to the leading 'extra jet' p_{T}. In the top panel, the unfolded data are shown as black points, while lines indicate the predictions from several MC programmes. Uncertainties are shown by the shaded bands. The lower two panels show the ratio of the MC predictions to the unfolded data. Fractional uncertainties (b) for the normalised single-differential cross-sections as a function of the ratio of sub-leading 'extra jet' p_{T} to the leading 'extra jet' p_{T}. The bands represent the uncertainties on the unfolded data. Lines indicate the breakdown of the major components of the uncertainties.

In the all-hadronic channel, the leading jet is also the leading parton-level object, which cannot be identified unambiguously in other decay channels (as this could be a neutrino). Figure 14 shows the separation in ΔR between the first emission and the leading jet in the event, which may or may not originate from the decay of one of the top quarks. A significant peak is observed at 0, demonstrating that in events with at least one extra jet the leading jet is most often from ISR rather than a top-quark decay product. The distribution of ΔR for events in which the leading jet is associated with one of the top quarks has a tendency towards large values, close to π, implying that the first emission in such cases is more aligned with the sub-leading top quark.

Significant mismodelling of this distribution is observed in Sherpa, MadGraph5_aMC@NLO+Pythia8 and Powheg+Herwig7, all of which underestimate how frequently the leading jet is a decay product of one of the top quarks. For such events, the extra jet is also typically emitted too close to the leading top quark. The same trend is seen to a lesser degree for the nominal Powheg+Pythia8 configuration, whereas the `Var3cUp` variation reproduces the data well.

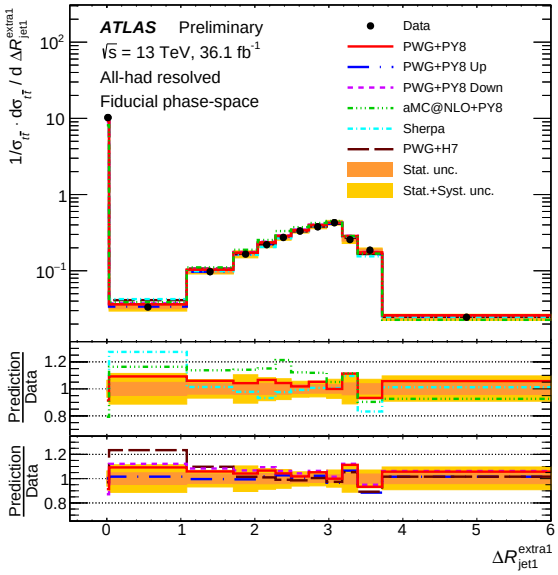

Figure 14: Particle-level normalised single-differential cross-section as a function of the geometric separation ΔR between the leading 'extra jet' and leading jet. In the top panel, the unfolded data are shown as black points, while lines indicate the predictions from several MC programmes. Uncertainties are shown by the shaded bands. The lower two panels show the ratio of the MC predictions to the unfolded data.

Normalised double-differential cross-sections as a function of the sub-leading top-quark p_{T} and the p_{T} of the $t\bar{t}$ system in bins of jet multiplicity are presented in Figures 15 and 16, respectively. For low jet multiplicities, which are relatively pure in signal, the dominant uncertainties are from jet energy scales, PDFs and the modelling of the $t\bar{t}$ radiation. As the parton shower modelling is particularly important at larger jet multiplicities, the corresponding uncertainty grows to be the most significant for both observables.

In both observables, the six- and seven-jet bins show the clearest signs of mismodelling. The MC predictions tend to be too hard for the sub-leading top-quark p_{T}, as was observed in the single-differential measurement. For the $t\bar{t}$ transverse momentum, on the other hand, different trends are seen, where the predictions are typically too soft in the seven-jet bin, where a single hard emission is produced, but too hard in the other bins.

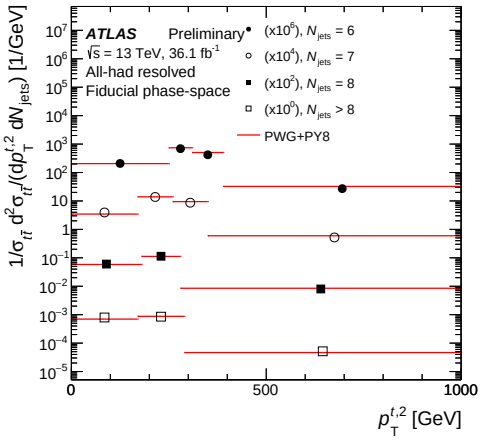

(a)

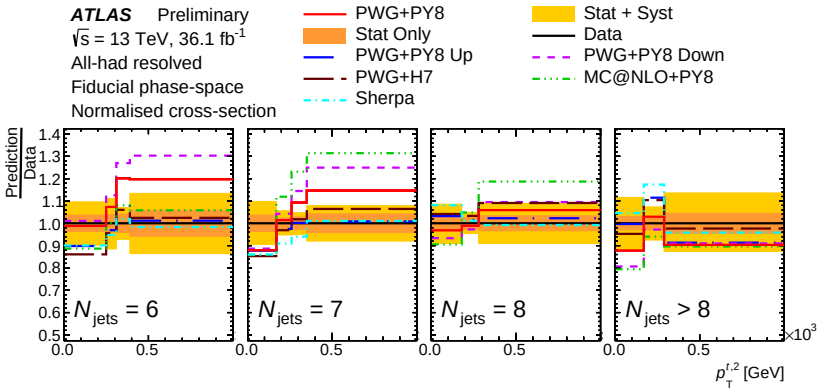

(b)

Figure 15: Particle-level double-differential normalised cross-section (a) as a function of the sub-leading top-quark transverse momentum $p_{\mathrm{T}}^{t,2}$ in bins of the jet multiplicity N_{jets}, compared to the nominal Powheg+Pythia8 prediction without uncertainties. Different markers are used to distinguish the four bins in N_{jets}, while $p_{\mathrm{T}}^{t,2}$ is shown on the x-axis. The ratio (b) of the measured cross-section to different MC predictions. Uncertainties are shown by the shaded bands.

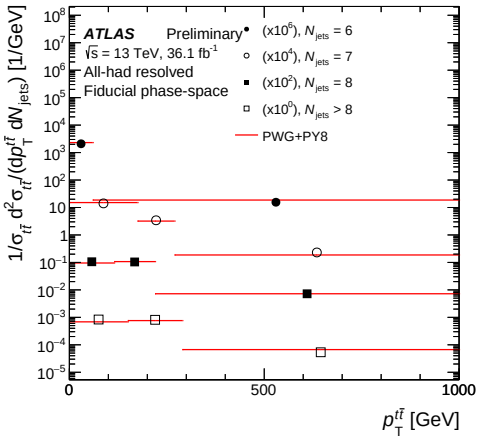

(a)

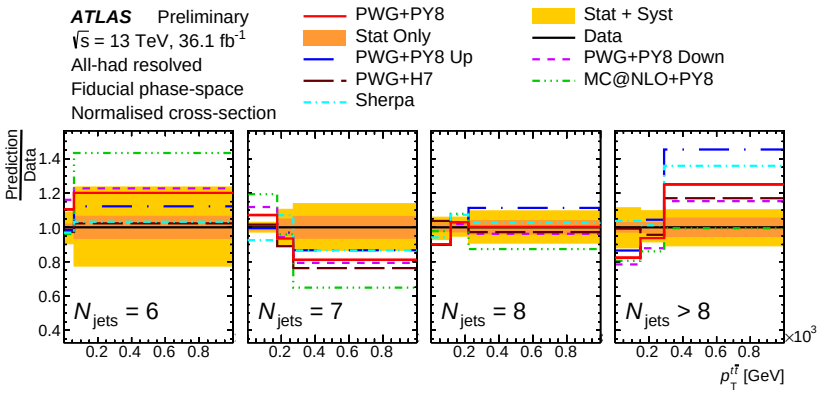

(b)

Figure 16: Particle-level double-differential normalised cross-section (a) as a function of the $t\bar{t}$ system transverse momentum $p_{\mathrm{T}}^{t\bar{t}}$ in bins of the jet multiplicity N_{jets}, compared to the nominal POWHEG+PYTHIA8 prediction without uncertainties. Different markers are used to distinguish the four bins in N_{jets}, while $p_{\mathrm{T}}^{t\bar{t}}$ is shown on the x-axis. The ratio (b) of the measured cross-section to different MC predictions. Uncertainties are shown by the shaded bands.

10.2.2 Results at parton level in the full phase space

At parton level, the normalised single-differential cross-section unfolded to the full phase space as a function of the transverse momentum of the leading top quark is presented in Figure 17. The corresponding absolute differential cross-section is shown in Figure 18 for comparison. The normalised measurement is once more characterised by significant cancellations in the uncertainties (primarily the b-tagging and parton shower ones). However the normalisation procedure inflates the hard scatter uncertainty at large p_{T}, due to the normalisation being influenced mostly by bins at low transverse momentum for which the absolute differential cross-section is affected by a large hard scatter uncertainty. Even so, the trends are similar to those observed in the particle-level measurements, with the data being best described by POWHEG+HERWIG7.

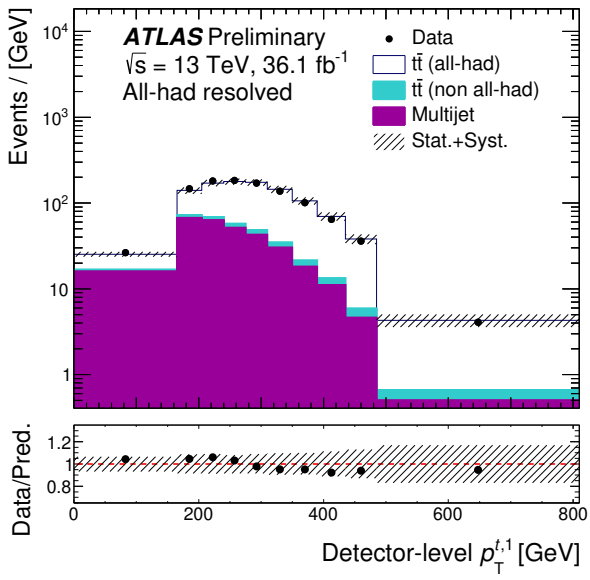

(a)

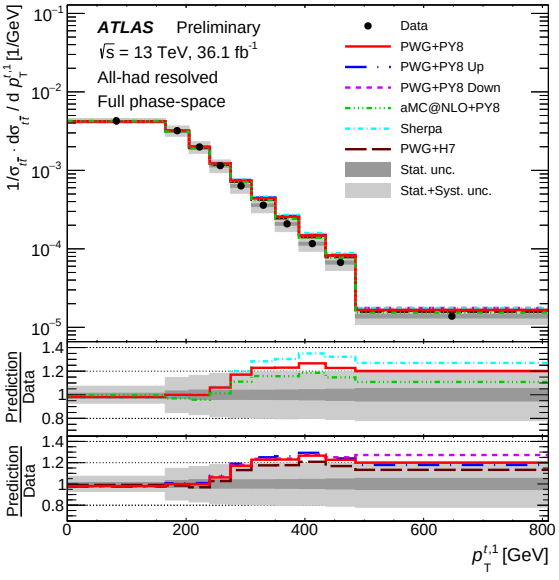

(b)

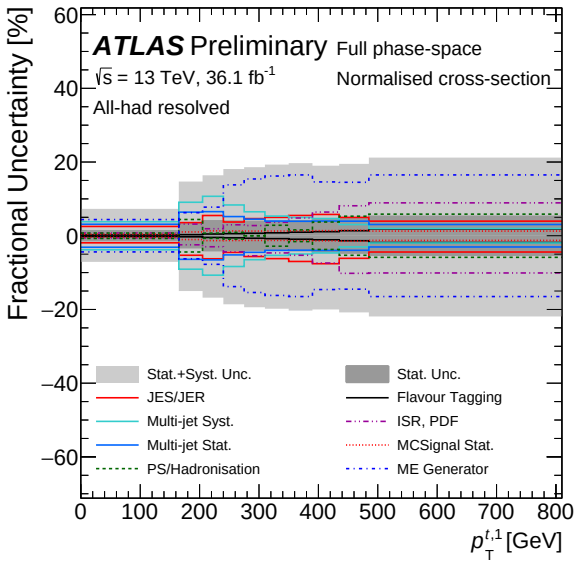

(c)

Figure 17: Comparison of the ATLAS data to the fully simulated nominal SM predictions (a) for the leading top-quark transverse momentum. The shaded bands represent the uncertainties on the total prediction. Data points are placed at the centre of each bin. The lower panel shows the ratios of the theoretical predictions to data. Single-differential normalised cross-section measurements, unfolded at parton level (b), as a function of the leading top-quark transverse momentum. The unfolded data are compared to theoretical predictions. In the top panel, the unfolded data are shown as black points, while lines indicate the predictions from several MC programmes. Uncertainties are shown by the shaded bands. The lower two panels show the ratio of the MC predictions to the unfolded data. Fractional uncertainties for the normalised single-differential distributions unfolded at parton level (c) as a function of the leading top-quark transverse momentum. The bands represent the uncertainties on the unfolded data. Lines indicate the breakdown of the major components of the uncertainties.

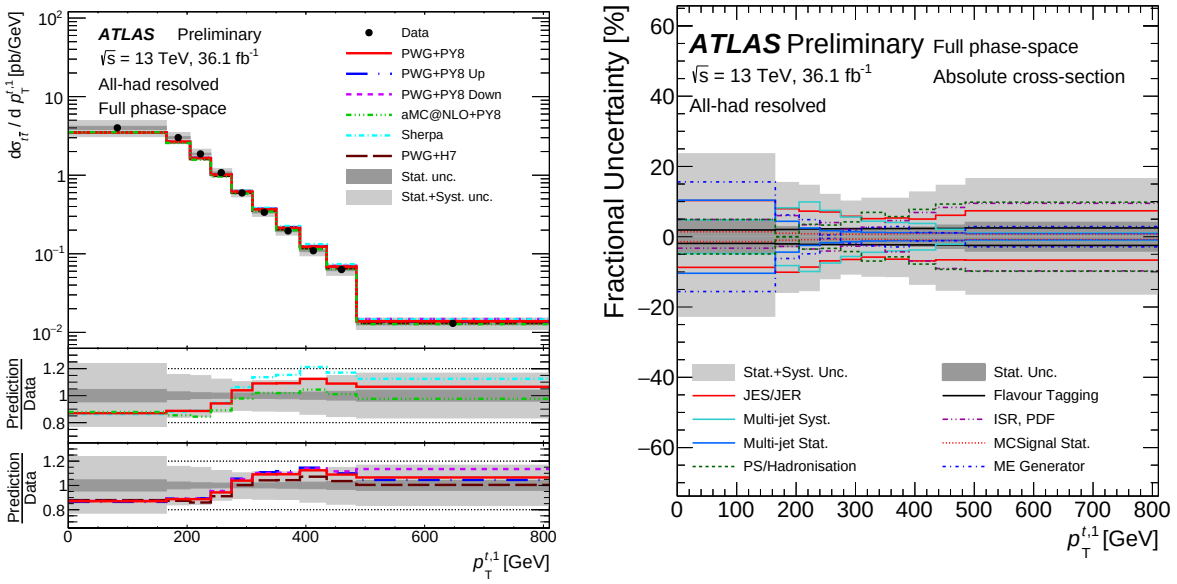

(a) (b)

Figure 18: Single-differential absolute cross-section measurements, unfolded at parton level (a), as a function of the leading top-quark transverse momentum. The unfolded data are compared to theoretical predictions. In the top panel, the unfolded data are shown as black points, while lines indicate the predictions from several MC programmes. Uncertainties are shown by the shaded bands. The lower two panels show the ratio of the MC predictions to the unfolded data. Fractional uncertainties for the absolute single-differential distributions unfolded at parton level (b) as a function of the leading top-quark transverse momentum. The bands represent the uncertainties on the unfolded data. Lines indicate the breakdown of the major components of the uncertainties.

The double-differential cross-section measurement of the leading top-quark transverse momentum versus the top-quark pair mass is shown in Figure 19. The main trend that is observed in this distributions is once more that the event generators predict a harder leading top-quark p_{T} than the data. This feature appears in all $m^{t\bar{t}}$ bins.

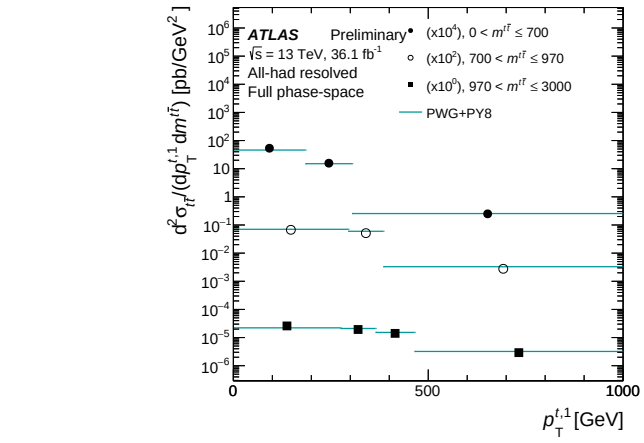

(a)

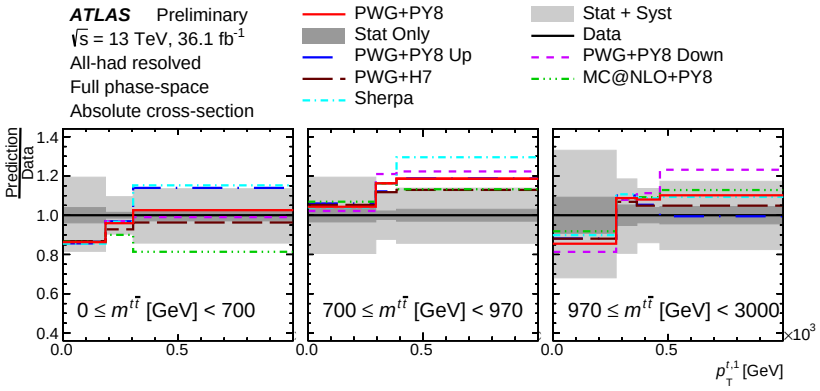

(b)

Figure 19: Parton-level double-differential absolute cross-section (a) as a function of the leading top-quark transverse momentum in bins of the $t\bar{t}$ system mass, compared to the nominal POWHEG+PYTHIA8 prediction without uncertainties. Different markers are used to distinguish the three bins in $m^{t\bar{t}}$, while $p_{\mathrm{T}}^{t,1}$ is shown on the x-axis. The ratio (b) of the measured cross-section to different MC predictions. Uncertainties are shown by the shaded bands.

10.3 Total cross-section

The total cross section is measured in the fiducial phase space and is compared with the MC predictions described previously, as shown in Figure 20 and in Table 16. The total cross section as predicted by each NLO MC generator is normalised to the NNLO+NNLL prediction as quoted in Ref. [45]. The corresponding uncertainty includes only the uncertainty affecting the k-factor used in the normalisation.

The total cross section in the full phase space, accounting for all decay modes, and it is found to be $\sigma_{t\bar{t}}$ = $864^{\pm 127}$(stat. + syst.) pb with a total uncertainty of 13%, to be compared with $\sigma_{t\bar{t}}$ = 832^{+20}_{-29}(scale) $\pm$

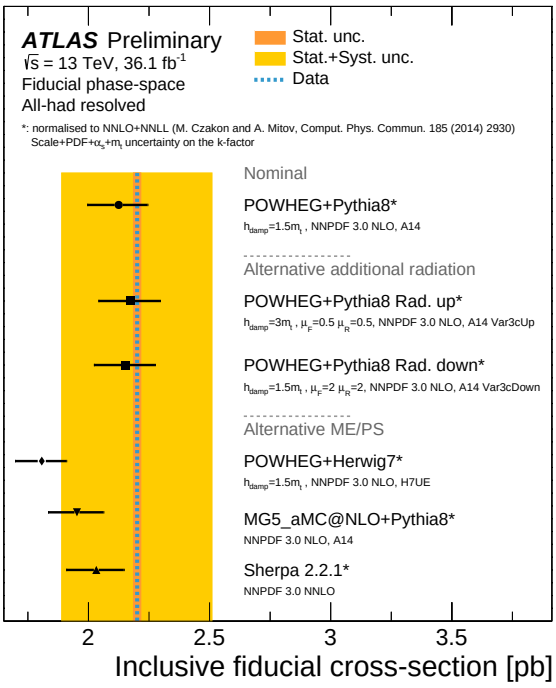

Figure 20: Comparison of the measured inclusive fiducial cross section with the predictions from several MC generators. The bands represent the statistical and total uncertainty in the data. The uncertainty on the cross-section predicted by each NLO MC generator only includes the uncertainty (due to PDFs, m_t and α_s) affecting the k-factor used in the normalisation.

Sample	Fiducial cross section [pb]
PWG+PY8	$2.13^{+0.13}_{-0.12}$
PWG+PY8 Rad. Up	$2.17^{+0.13}_{-0.12}$
PWG+PY8 Rad. Down	$2.15^{+0.13}_{-0.12}$
PWG+H7	$1.81^{+0.11}_{-0.10}$
MADGRAPH5_aMC@NLO	$1.95^{+0.12}_{-0.11}$
SHERPA 2.2.1	$2.03^{+0.12}_{-0.11}$
Data	2.20 ± 0.31(stat. + syst.)

Table 16: Comparison of the measured inclusive fiducial cross-section with the predictions from several MC generators.

35 (PDF, α_S) pb as calculated with the Top++2.0 program at NNLO in perturbative QCD, including soft-gluon resummation to NNLL [21, 45–50], and assuming m_t = 172.5 GeV.

10.4 Consistency with other differential cross-section measurements

10.4.1 Comparison of results with ℓ+jets channel

Many of the observables measured in this paper were also measured in the ℓ+jets final state of the top-quark pair production [3]. Before comparing the results, it is important to note that there are several differences between the two approaches. The object selection, which is driven by the triggers, is significantly different since the results presented in this paper are based on a selection of at least six jets with a p_{T} greater than 55 GeV while the ℓ+jets analysis requires a lepton with $p_{\mathrm{T}} > 20$ GeV and all jets to have $p_{\mathrm{T}} > 25$ GeV. The extrapolation to the full phase space used in the parton-level results is therefore much bigger for the all-hadronic channel and the size of the available data sample is smaller. However, the all-hadronic channel allows for full event reconstruction from well measured objects, leading to better resolution on the observables and to particular angular distributions and measurements of 'extra jets' with respect to the top-quark pair system. These effects combine in non-trivial ways and it is therefore difficult to say a priori which analysis can provide the highest discrimination between models.

The particle-level results of both analyses are generally compatible in terms of the amount of agreement observed between data and predictions, with some differences identified where variables are better described in either the ℓ+jets channel or the all-hadronic channel. For example, consistent mismodelling is observed in both analyses for the $p_{\mathrm{T}}^{t\bar{t}}$ distribution. The $H_{\mathrm{T}}^{t\bar{t}}$ distribution is strongly correlated with the top-quark p_{T} distributions; it is poorly modelled by all the MC predictions in the all-hadronic channel while in the ℓ+jets channel a good agreement is observed between data and all the MC predictions. A mismodelling between data and some of the MC predictions is observed for the $m^{t\bar{t}}$ observable in the all-hadronic channel, while, a good modelling is observed for this variable in the ℓ+jets channel. The ℓ+jets channel observed a mismodelling in $\Delta\phi^{t\bar{t}}$ for some MC predictions, whereas in the all-hadronic channel this mismodelling is not apparent in the single-differential distribution.

At parton level, the $p_{\mathrm{T}}^{t\bar{t}}$ and the $m^{t\bar{t}}$ are poorly described by most of the MC predictions in both the ℓ+jets and all-hadronic channels. However, a good agreement between data and all the MC predictions is observed in both channels for the $H_{\mathrm{T}}^{t\bar{t}}$ variable.

When considering the double-differential results at both particle and parton levels, both analyses show that none of the predictions can describe any of the measured distributions.

Figure 21 shows a comparison between the measured absolute differential cross-sections in the ℓ+jets and in the all-hadronic channels, at parton level, for the $H_{\mathrm{T}}^{t\bar{t}}$ and average top transverse momentum p_{T}^{t}. The two measurements are qualitatively consistent in the overlap region.

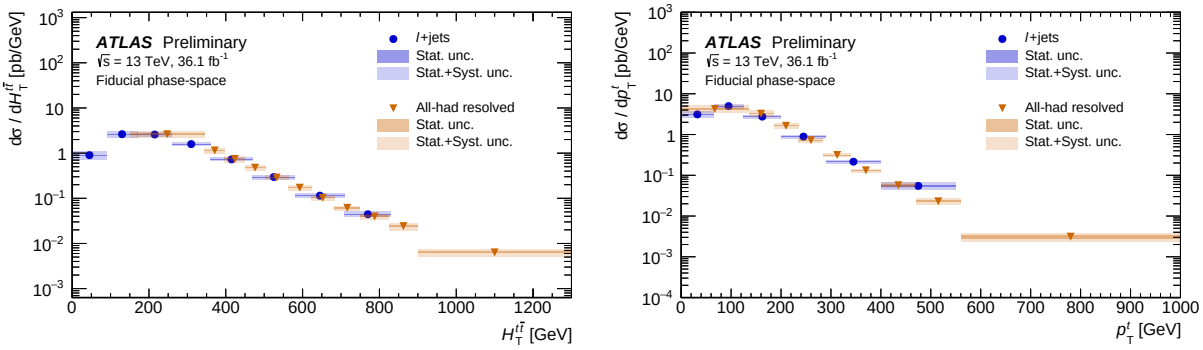

(a) (b)

Figure 21: Comparison between the measured absolute single-differential cross-sections in the ℓ+jets and all-hadronic channel as a function of the (a) $H_{\mathrm{T}}^{t\bar{t}}$ variable and as a function of the average top transverse momentum (b) p_{T}^{t}. The latter is determined by randomly picking one of the two top candidates in each event.

10.4.2 Comparison of results with the all-hadronic channel in the boosted topology

Measurements of differential cross-sections in the all-hadronic channel have been performed in the boosted topology [17], motivating a comparison to the results of this analysis. The all-hadronic resolved parton level measurements are unfolded to the full phase space, while the measurements in the boosted topology are unfolded to a fiducial phase space, therefore, a direct comparison of the differential measurements is not possible. Instead, Figure 22 shows the ratios of the measured absolute differential cross-sections at parton level to the predictions obtained with the POWHEG+PYTHIA8 MC generator in the all-hadronic resolved and boosted topologies as a function of the $p_{\mathrm{T}}^{t,1}$ and $p_{\mathrm{T}}^{t,2}$ variables. It can be seen from the figures that the ratios between the data and the signal MC generator is consistent between the two topologies in the overlap region.

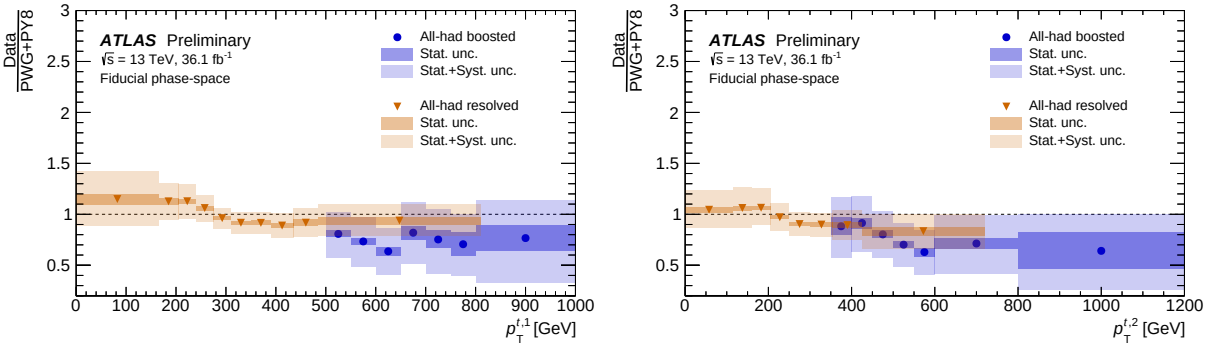

(a) (b)

Figure 22: The ratios of the measured absolute differential cross-sections at parton level to the predictions obtained with the POWHEG+PYTHIA8 MC generator in the all-hadronic resolved and boosted topologies as a function of the (a) $p_{\mathrm{T}}^{t,1}$ and (b) $p_{\mathrm{T}}^{t,2}$ variables.

11 Conclusions

A comprehensive measurement of single- and double-differential cross-sections for the production of top-quark pairs are performed in the all-hadronic channel, in the resolved topology using data from pp collisions at 13 TeV collected in 2015 and 2016 by the ATLAS detector at CERN LHC and corresponding to an integrated luminosity of 36 fb^{-1}.

Absolute and normalised differential cross-sections are presented as a function of several kinematic variables at particle and parton-level.

The results show sensitivity to different aspects of predictions made by the tested MC generators. As several predictions in a number of variables have a poor agreement with the data, these observations can be exploited to improve the top-quark MC modelling. In particular, the double differential cross-sections at particle level will be extremely useful for improving the MC predictions in regions of the phase space with many additional jets, which are a region of interest for analyses of many rare processes.

Several novel variables were introduced to better probe correlations between the kinematics of the top-quark pair and associated jet radiations which can be used to further improve the next generation of MC samples.

The measurements at parton level were compared with theory predictions obtained by NLO MC generators enriched with parton shower and hadronisation models and can also be used in future measurements such as PDF and top-quark pole mass extraction. The rapidities of the individual top quarks and of the top-quark pair are well modelled. In contrast, significant mismodelling is observed in the hardness of the leading three jet emissions, while the leading top-quark transverse momentum and top-quark pair transverse momentum are together found to be incompatible with several theoretical predictions.

Despite non-negligible backgrounds, an effective event selection and background estimation strategy permitted sufficiently precise measurements to constrain MC predictions in events with up to three additional jets. The major limitation on the analysis presented is the limited efficiency of the hadronic trigger selection. It is noted that future detector upgrades will improve the prospects for triggering on hadronic top-quark pair production, in particular by means of advances that permit the further use of tracking at trigger level, for jet calibration, pileup suppression and flavour-tagging. A multijet-plus-flavour-tag trigger signature is particularly motivated by the measurements presented here.

References

[1] L. Evans and P. Bryant, *LHC Machine*, JINST **3** (2008) S08001 (cit. on p. 2).

[2] ATLAS Collaboration, *The ATLAS Experiment at the CERN Large Hadron Collider*, JINST **3** (2008) S08003 (cit. on pp. 2, 3).

[3] ATLAS Collaboration, *Measurements of top-quark pair differential and double-differential cross-sections in the ℓ+jets channel with pp collisions at $\sqrt{s}$ = 13 TeV using the ATLAS detector*, (2019), arXiv: 1908.07305 [hep-ex] (cit. on pp. 2, 31, 49).

[4] CMS Collaboration, *Measurement of differential cross sections for the production of top quark pairs and of additional jets in lepton+jets events from pp collisions at $\sqrt{s}$ = 13 TeV*, Phys. Rev. D **97** (2018) 112003, arXiv: 1803.08856 [hep-ex] (cit. on p. 2).

[5] CMS Collaboration, *Measurements of differential cross sections of top quark pair production as a function of kinematic event variables in proton–proton collisions at* $\sqrt{s} = 13$ *TeV*, JHEP **06** (2018) 002, arXiv: 1803.03991 [hep-ex] (cit. on p. 2).

[6] ATLAS Collaboration, *Measurements of differential cross sections of top quark pair production in association with jets in pp collisions at* $\sqrt{s} = 13$ *TeV using the ATLAS detector*, JHEP **10** (2018) 159, arXiv: 1802.06572 [hep-ex] (cit. on p. 2).

[7] ATLAS Collaboration, *Measurement of the inclusive and fiducial* $t\bar{t}$ *production cross-sections in the lepton+jets channel in pp collisions at* $\sqrt{s} = 8$ *TeV with the ATLAS detector*, Eur. Phys. J. C **78** (2018) 487, arXiv: 1712.06857 [hep-ex] (cit. on p. 2).

[8] CMS Collaboration, *Measurement of normalized differential* $t\bar{t}$ *cross sections in the dilepton channel from pp collisions at* $\sqrt{s} = 13$ *TeV*, JHEP **04** (2018) 060, arXiv: 1708.07638 [hep-ex] (cit. on p. 2).

[9] ATLAS Collaboration, *Measurement of lepton differential distributions and the top quark mass in* $t\bar{t}$ *production in pp collisions at* $\sqrt{s} = 8$ *TeV with the ATLAS detector*, Eur. Phys. J. C **77** (2017) 804, arXiv: 1709.09407 [hep-ex] (cit. on p. 2).

[10] CMS Collaboration, *Measurement of double-differential cross sections for top quark pair production in pp collisions at* $\sqrt{s} = 8$ *TeV and impact on parton distribution functions*, Eur. Phys. J. C **77** (2017) 459, arXiv: 1703.01630 [hep-ex] (cit. on p. 2).

[11] ATLAS Collaboration, *Measurements of top-quark pair differential cross-sections in the* $e\mu$ *channel in pp collisions at* $\sqrt{s} = 13$ *TeV using the ATLAS detector*, Eur. Phys. J. C **77** (2017) 292, arXiv: 1612.05220 [hep-ex] (cit. on p. 2).

[12] CMS Collaboration, *Measurement of differential cross sections for top quark pair production using the lepton+jets final state in proton–proton collisions at* 13 *TeV*, Phys. Rev. D **95** (2017) 092001, arXiv: 1610.04191 [hep-ex] (cit. on p. 2).

[13] ATLAS Collaboration, *Measurements of top-quark pair differential cross-sections in the lepton+jets channel in pp collisions at* $\sqrt{s} = 8$ *TeV using the ATLAS detector*, Eur. Phys. J. C **76** (2016) 538, arXiv: 1511.04716 [hep-ex] (cit. on pp. 2, 15).

[14] CMS Collaboration, *Measurement of the integrated and differential* $t\bar{t}$ *production cross sections for high-*p_T *top quarks in pp collisions at* $\sqrt{s} = 8$ *TeV*, Phys. Rev. D **94** (2016) 072002, arXiv: 1605.00116 [hep-ex] (cit. on p. 2).

[15] CMS Collaboration, *Measurement of the* $t\bar{t}$ *production cross section in the all-jets final state in pp collisions at* $\sqrt{s} = 8$ *TeV*, Eur. Phys. J. C **76** (2016) 128, arXiv: 1509.06076 [hep-ex] (cit. on p. 2).

[16] CMS Collaboration, *Measurement of the* $t\bar{t}$ *production cross section in the all-jet final state in pp collisions at* $\sqrt{s} = 7$ *TeV*, JHEP **05** (2013) 065, arXiv: 1302.0508 [hep-ex] (cit. on p. 2).

[17] ATLAS Collaboration, *Measurements of* $t\bar{t}$ *differential cross-sections of highly boosted top quarks decaying to all-hadronic final states in pp collisions at* $\sqrt{s} = 13$ *TeV using the ATLAS detector*, Phys. Rev. D **98** (2018) 012003, arXiv: 1801.02052 [hep-ex] (cit. on pp. 2, 9, 14, 15, 50).

[18] P. Nason, *A New method for combining NLO QCD with shower Monte Carlo algorithms*, JHEP **11** (2004) 040, arXiv: hep-ph/0409146 [hep-ph] (cit. on p. 2).

[19] S. Frixione, P. Nason and C. Oleari, *Matching NLO QCD computations with parton shower simulations: the POWHEG method*, JHEP **11** (2007) 070, arXiv: 0709.2092 [hep-ph] (cit. on pp. 2, 4).

[20] S. Alioli, P. Nason, C. Oleari and E. Re, *A general framework for implementing NLO calculations in shower Monte Carlo programs: the POWHEG BOX*, JHEP **06** (2010) 043, arXiv: 1002.2581 [hep-ph] (cit. on pp. 2, 4).

[21] S. Alioli, S.-O. Moch and P. Uwer, *Hadronic top-quark pair-production with one jet and parton showering*, JHEP **01** (2012) 137, arXiv: 1110.5251 [hep-ph] (cit. on pp. 2, 5, 48).

[22] J. Alwall et al., *The automated computation of tree-level and next-to-leading order differential cross sections, and their matching to parton shower simulations*, JHEP **07** (2014) 079, arXiv: 1405.0301 [hep-ph] (cit. on pp. 2, 5).

[23] T. Sjöstrand, S. Mrenna and P. Z. Skands, *A brief introduction to PYTHIA 8.1*, Comput. Phys. Commun. **178** (2008) 852, arXiv: 0710.3820 [hep-ph] (cit. on pp. 2, 4).

[24] J. Bellm et al., *Herwig 7.0/Herwig++ 3.0 release note*, Eur. Phys. J. **C76** (2016) 196, arXiv: 1512.01178 [hep-ph] (cit. on pp. 2, 5).

[25] T. Gleisberg et al., *Event generation with SHERPA 1.1*, JHEP **02** (2009) 007, arXiv: 0811.4622 [hep-ph] (cit. on pp. 2, 4, 5).

[26] ATLAS Collaboration, *Performance of the ATLAS trigger system in 2015*, Eur. Phys. J. C **77** (2017) 317, arXiv: 1611.09661 [hep-ex] (cit. on p. 3).

[27] ATLAS Collaboration, *Luminosity determination in pp collisions at $\sqrt{s}$ = 13 TeV using the ATLAS detector at the LHC*, ATLAS-CONF-2019-021, 2019, URL: https://cds.cern.ch/record/2677054 (cit. on pp. 3, 21).

[28] G. Avoni et al., *The new LUCID-2 detector for luminosity measurement and monitoring in ATLAS*, JINST **13** (2018) P07017 (cit. on p. 3).

[29] M. Cacciari, G. P. Salam and G. Soyez, *The Anti-k_t jet clustering algorithm*, JHEP **04** (2008) 063, arXiv: 0802.1189 [hep-ph] (cit. on p. 3).

[30] D. J. Lange, *The EvtGen particle decay simulation package*, Nucl. Instrum. Meth. A **462** (2001) 152 (cit. on p. 4).

[31] ATLAS Collaboration, *The Pythia 8 A3 tune description of ATLAS minimum bias and inelastic measurements incorporating the Donnachie–Landshoff diffractive model*, ATL-PHYS-PUB-2016-017, 2016, URL: https://cds.cern.ch/record/2206965 (cit. on p. 4).

[32] R. D. Ball et al., *Parton distributions with LHC data*, Nucl. Phys. B **867** (2013) 244, arXiv: 1207.1303 [hep-ph] (cit. on p. 4).

[33] S. Agostinelli et al., *Geant4 a simulation toolkit*, Nucl. Instrum. Meth. A **506** (2003) (cit. on p. 4).

[34] ATLAS Collaboration, *The ATLAS Simulation Infrastructure*, Eur. Phys. J. C **70** (2010) 823, arXiv: 1005.4568 [physics.ins-det] (cit. on p. 4).

[35] R. D. Ball et al., *Parton distributions for the LHC Run II*, JHEP **04** (2015) 040, arXiv: 1410.8849 [hep-ph] (cit. on p. 4).

[36] R. D. Ball et al., *Parton distributions with LHC data*, Nucl. Phys. B **867** (2013) 244, arXiv: 1207.1303 [hep-ex] (cit. on pp. 4, 5).

[37] ATLAS Collaboration, *ATLAS Pythia 8 tunes to 7 TeV data*, ATL-PHYS-PUB-2014-021, 2014, URL: https://cds.cern.ch/record/1966419 (cit. on p. 4).

[38] ATLAS Collaboration, *Simulation of top-quark production for the ATLAS experiment at $\sqrt{s}$ = 13 TeV*, ATL-PHYS-PUB-2016-004, 2016, URL: https://cds.cern.ch/record/2120417 (cit. on p. 4).

[39] M. Bahr et al., *Herwig++ physics and manual*, Eur. Phys. J. C **58** (2008) 639, arXiv: 0803.0883 [hep-ph] (cit. on p. 5).

[40] M. H. Seymour and A. Siódmok, *Constraining MPI models using σ_{eff} and recent Tevatron and LHC Underlying Event data*, JHEP **2013** (2013) 113, ISSN: 1029-8479, URL: https://doi.org/10.1007/JHEP10(2013)113 (cit. on p. 5).

[41] ATLAS Collaboration, *Performance of the Fast ATLAS Tracking Simulation (FATRAS) and the ATLAS Fast Calorimeter Simulation (FastCaloSim) with single particles*, ATL-SOFT-PUB-2014-01, 2014, URL: https://cds.cern.ch/record/1669341 (cit. on p. 5).

[42] ATLAS Collaboration, *Studies on top-quark Monte Carlo modelling with Sherpa and MG5_aMC@NLO*, ATL-PHYS-PUB-2017-007, 2017, URL: https://cds.cern.ch/record/2261938 (cit. on p. 5).

[43] S. Höche, F. Krauss, M. Schönherr and F. Siegert, *QCD matrix elements + parton showers: The NLO case*, JHEP **04** (2013) 027, arXiv: 1207.5030 [hep-ph] (cit. on p. 5).

[44] F. Cascioli, P. Maierhofer and S. Pozzorini, *Scattering Amplitudes with Open Loops*, Phys. Rev. Lett. **108** (2012) 111601, arXiv: 1111.5206 [hep-ph] (cit. on p. 5).

[45] M. Czakon and A. Mitov, *Top++: A program for the calculation of the top-pair cross-section at hadron colliders*, Comput. Phys. Commun. **185** (2014) 2930, arXiv: 1112.5675 [hep-ph] (cit. on pp. 5, 47, 48).

[46] M. Czakon et al., *Top-pair production at the LHC through NNLO QCD and NLO EW*, JHEP **10** (2017) 186, arXiv: 1705.04105 [hep-ph] (cit. on pp. 5, 48).

[47] P. Barnreuther, M. Czakon and A. Mitov, *Percent-Level-Precision Physics at the Tevatron: Next-to-Next-to-Leading Order QCD Corrections to $q\bar{q} \to t\bar{t}+X$*, Phys. Rev. Lett. **109** (2012) 132001, arXiv: 1204.5201 [hep-ph] (cit. on pp. 5, 48).

[48] M. Czakon and A. Mitov, *NNLO corrections to top-pair production at hadron colliders: the all-fermionic scattering channels*, JHEP **12** (2012) 054, arXiv: 1207.0236 [hep-ph] (cit. on pp. 5, 48).

[49] M. Czakon and A. Mitov, *NNLO corrections to top pair production at hadron colliders: the quark-gluon reaction*, JHEP **01** (2013) 080, arXiv: 1210.6832 [hep-ph] (cit. on pp. 5, 48).

[50] M. Czakon, P. Fiedler and A. Mitov, *Total Top-Quark Pair-Production Cross Section at Hadron Colliders Through $O(\alpha_s^4)$*, Phys. Rev. Lett. **110** (2013) 252004, arXiv: 1303.6254 [hep-ph] (cit. on pp. 5, 48).

[51] A. D. Martin, W. J. Stirling, R. S. Thorne and G. Watt, *Uncertainties on α_s in global PDF analyses and implications for predicted hadronic cross sections*, Eur. Phys. J. C **64** (2009) 653, arXiv: 0905.3531 [hep-ph] (cit. on p. 5).

[52] H.-L. Lai et al., *New parton distributions for collider physics*, Phys. Rev. D **82** (2010) 074024, arXiv: 1007.2241 [hep-ph] (cit. on p. 5).

[53] J. Butterworth et al., *PDF4LHC recommendations for LHC Run II*, J. Phys. G **43** (2016) 023001, arXiv: 1510.03865 [hep-ph] (cit. on pp. 5, 22).

[54] ATLAS Collaboration, *Topological cell clustering in the ATLAS calorimeters and its performance in LHC Run 1*, Eur. Phys. J. C **77** (2017) 490, arXiv: 1603.02934 [hep-ex] (cit. on p. 5).

[55] M. Cacciari, G. P. Salam and G. Soyez, *FastJet user manual*, Eur. Phys. J. C **72** (2012) 1896, arXiv: 1111.6097 [hep-ph] (cit. on p. 6).

[56] M. Cacciari and G. P. Salam, *Pileup subtraction using jet areas*, Phys. Lett. B **659** (2008) 119, arXiv: 0707.1378 [hep-ph] (cit. on p. 6).

[57] ATLAS Collaboration, *Jet energy scale measurements and their systematic uncertainties in proton–proton collisions at $\sqrt{s}$ = 13 TeV with the ATLAS detector*, Phys. Rev. D **96** (2017) 072002, arXiv: 1703.09665 [hep-ex] (cit. on pp. 6, 20).

[58] ATLAS Collaboration, *Performance of pile-up mitigation techniques for jets in pp collisions at $\sqrt{s}$ = 8 TeV using the ATLAS detector*, Eur. Phys. J. C **76** (2016) 581, arXiv: 1510.03823 [hep-ex] (cit. on p. 6).

[59] M. Cacciari, G. P. Salam and G. Soyez, *The catchment area of jets*, JHEP **04** (2008) 005, arXiv: 0802.1188 [hep-ph] (cit. on p. 6).

[60] ATLAS Collaboration, *Optimisation of the ATLAS b-tagging performance for the 2016 LHC Run*, ATL-PHYS-PUB-2016-012, 2016, URL: https://cds.cern.ch/record/2160731 (cit. on p. 6).

[61] ATLAS Collaboration, *Performance of b-jet identification in the ATLAS experiment*, JINST **11** (2016) P04008, arXiv: 1512.01094 [hep-ex] (cit. on p. 6).

[62] ATLAS Collaboration, *Electron and photon energy calibration with the ATLAS detector using 2015–2016 LHC proton–proton collision data*, JINST **14** (2019) P03017, arXiv: 1812.03848 [hep-ex] (cit. on p. 6).

[63] ATLAS Collaboration, *Electron reconstruction and identification in the ATLAS experiment using the 2015 and 2016 LHC proton–proton collision data at $\sqrt{s}$ = 13 TeV*, Eur. Phys. J. C **79** (2019) 639, arXiv: 1902.04655 [hep-ex] (cit. on p. 6).

[64] ATLAS Collaboration, *Expected electron performance in the ATLAS experiment*, ATL-PHYS-PUB-2011-006, 2011, URL: https://cds.cern.ch/record/1345327 (cit. on p. 6).

[65] ATLAS Collaboration, *Muon reconstruction performance of the ATLAS detector in proton–proton collision data at $\sqrt{s}$ = 13 TeV*, Eur. Phys. J. C **76** (2016) 292, arXiv: 1603.05598 [hep-ex] (cit. on p. 6).

[66] ATLAS Collaboration, *Reconstruction, Energy Calibration, and Identification of Hadronically Decaying Tau Leptons in the ATLAS Experiment for Run-2 of the LHC*, ATL-PHYS-PUB-2015-045, 2015, URL: https://cds.cern.ch/record/2064383 (cit. on p. 6).

[67] ATLAS Collaboration, *Measurement of the tau lepton reconstruction and identification performance in the ATLAS experiment using pp collisions at $\sqrt{s}$ = 13 TeV*, ATLAS-CONF-2017-029, 2017, URL: https://cds.cern.ch/record/2261772 (cit. on p. 6).

[68] C. Patrignani et al., *Review of Particle Physics*, Chin. Phys. C **40** (2016) 100001 (cit. on p. 8).

[69] ATLAS Collaboration, *Search for resonances decaying into top-quark pairs using fully hadronic decays in pp collisions with ATLAS at $\sqrt{s}$ = 7 TeV*, JHEP **01** (2013) 116, arXiv: 1211.2202 [hep-ex] (cit. on p. 9).

[70] ATLAS Collaboration, *Search for New Phenomena in Dijet Angular Distributions in Proton–Proton Collisions at $\sqrt{s}$ = 8 TeV Measured with the ATLAS Detector*, Phys. Rev. Lett. **114** (2015) 221802, arXiv: 1504.00357 [hep-ex] (cit. on p. 14).

[71] L. Apanasevich et al., *Evidence for Parton k_T Effects in High- p_T Particle Production*, Phys. Rev. Lett. **81** (13 1998) 2642, URL: https://link.aps.org/doi/10.1103/PhysRevLett.81.2642 (cit. on p. 14).

[72] G. D'Agostini, *A multidimensional unfolding method based on Bayes' theorem*, Nucl. Instrum. Meth. A **362** (1995) 487 (cit. on p. 16).

[73] T. Adye, *Unfolding algorithms and tests using RooUnfold*, 2011, arXiv: 1105.1160 [physics.data-an] (cit. on p. 16).

[74] ATLAS Collaboration, *Jet energy measurement and its systematic uncertainty in proton–proton collisions at $\sqrt{s}$ = 7 TeV with the ATLAS detector*, Eur. Phys. J. C **75** (2015) 17, arXiv: 1406.0076 [hep-ex] (cit. on p. 20).

[75] ATLAS Collaboration, *Single hadron response measurement and calorimeter jet energy scale uncertainty with the ATLAS detector at the LHC*, Eur. Phys. J. C **73** (2013) 2305, arXiv: 1203.1302 [hep-ex] (cit. on p. 20).

[76] ATLAS Collaboration, *Jet Calibration and Systematic Uncertainties for Jets Reconstructed in the ATLAS Detector at $\sqrt{s}$ = 13 TeV*, ATL-PHYS-PUB-2015-015, 2015, URL: https://cds.cern.ch/record/2037613 (cit. on p. 20).

[77] ATLAS Collaboration, *Tagging and suppression of pileup jets with the ATLAS detector*, ATLAS-CONF-2014-018, 2014, URL: https://cds.cern.ch/record/1700870 (cit. on p. 20).

[78] ATLAS Collaboration, *Secondary vertex finding for jet flavour identification with the ATLAS detector*, ATL-PHYS-PUB-2017-011, 2017, URL: https://cds.cern.ch/record/2270366 (cit. on p. 21).

Auxiliary material

A Particle-level results in the fiducial phase-space

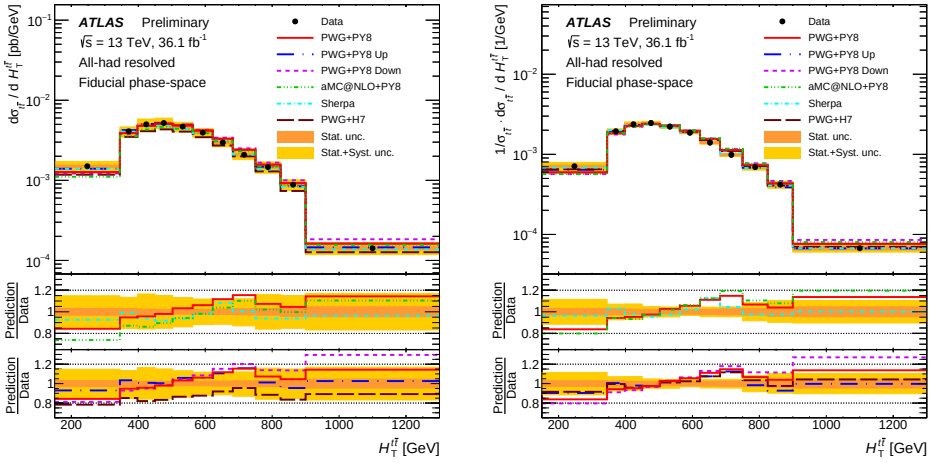

Figure 23: Differential cross sections in the fiducial phase-space as a function of $H_{\mathrm{T}}^{t\bar{t}}$: absolute (a) and normalised (b). The shaded area represents the total statistical and systematic uncertainties.

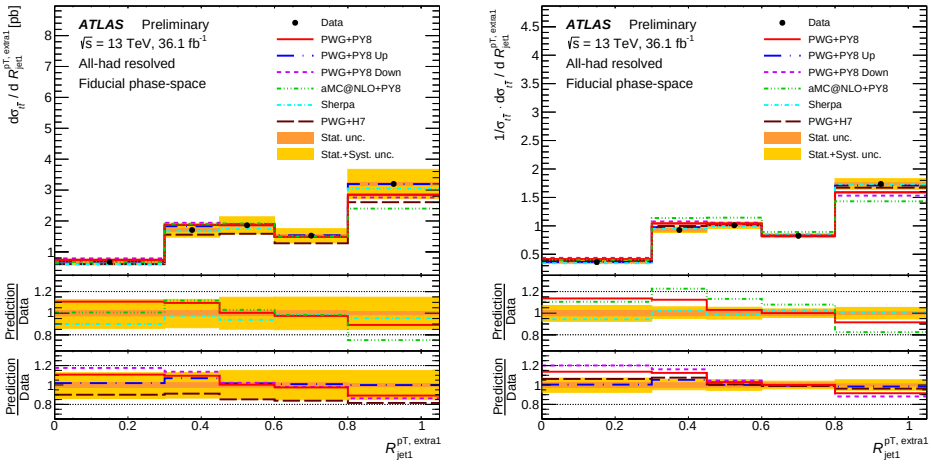

Figure 24: Differential cross sections in the fiducial phase-space as a function of $R_{\mathrm{jet1}}^{\mathrm{extra1}}$: absolute (a) and normalised (b). The shaded area represents the total statistical and systematic uncertainties.

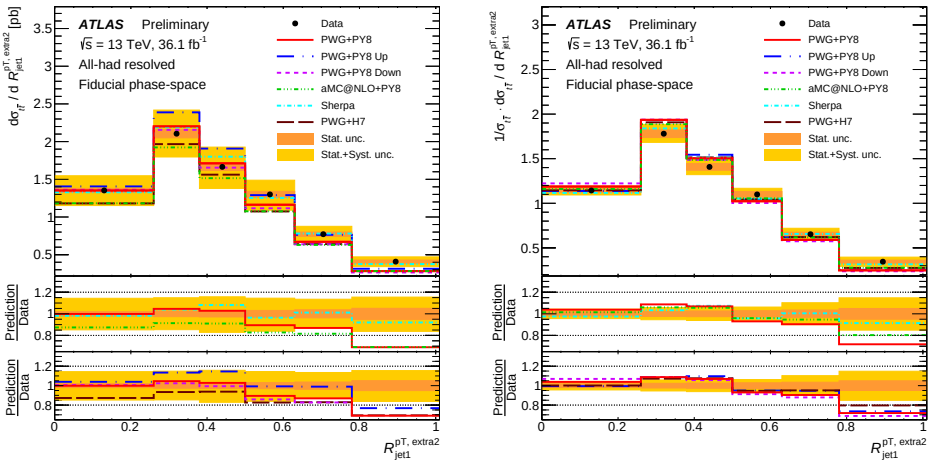

Figure 25: Differential cross sections in the fiducial phase-space as a function of $R_{\text{jet1}}^{\text{extra2}}$: absolute (a) and normalised (b). The shaded area represents the total statistical and systematic uncertainties.

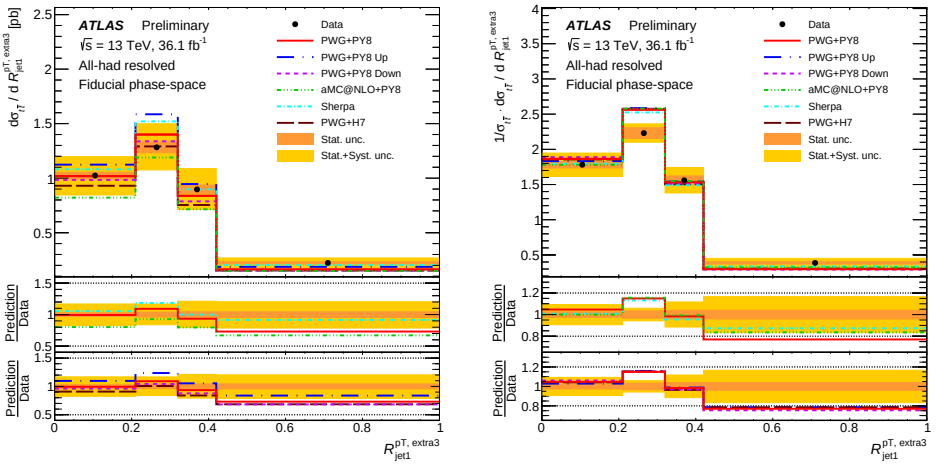

Figure 26: Differential cross sections in the fiducial phase-space as a function of $R_{\text{jet1}}^{\text{extra3}}$: absolute (a) and normalised (b). The shaded area represents the total statistical and systematic uncertainties.

B Parton-level results in the full phase-space

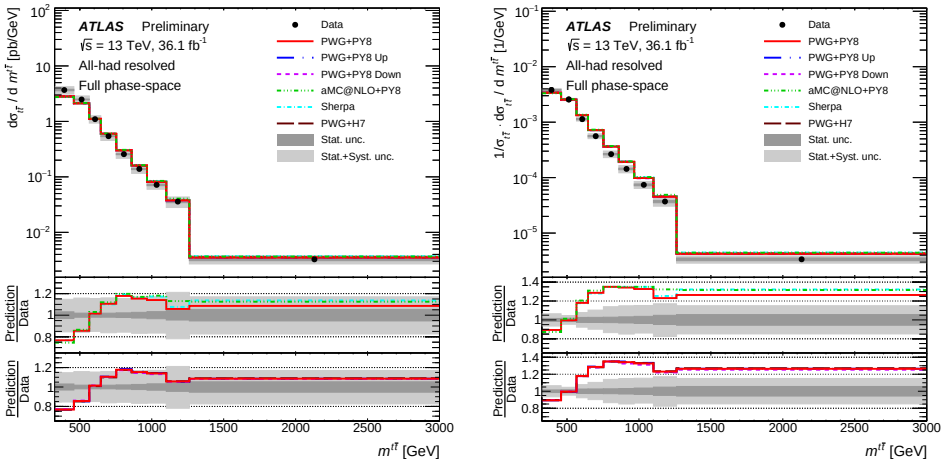

Figure 27: Differential cross sections in the full phase-space as a function of $m^{t\bar{t}}$: absolute (a) and normalised (b). The shaded area represents the total statistical and systematic uncertainties.

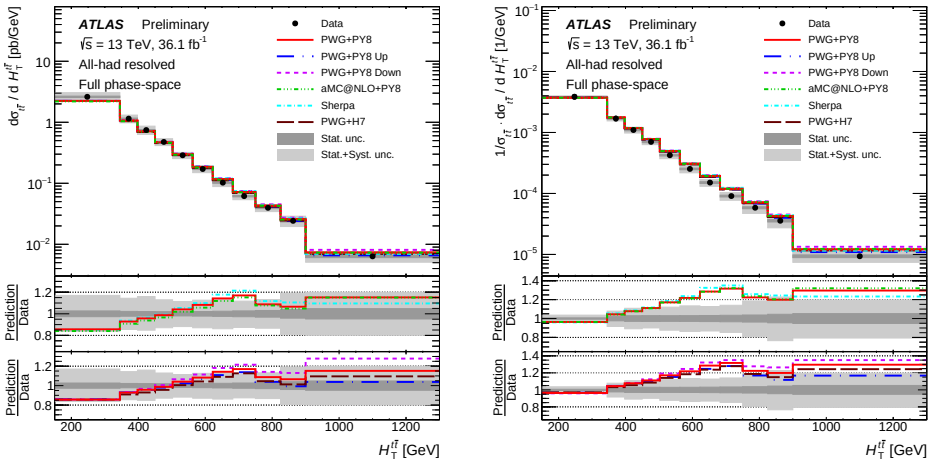

Figure 28: Differential cross sections in the full phase-space as a function of $H_{\mathrm{T}}^{t\bar{t}}$: absolute (a) and normalised (b). The shaded area represents the total statistical and systematic uncertainties.

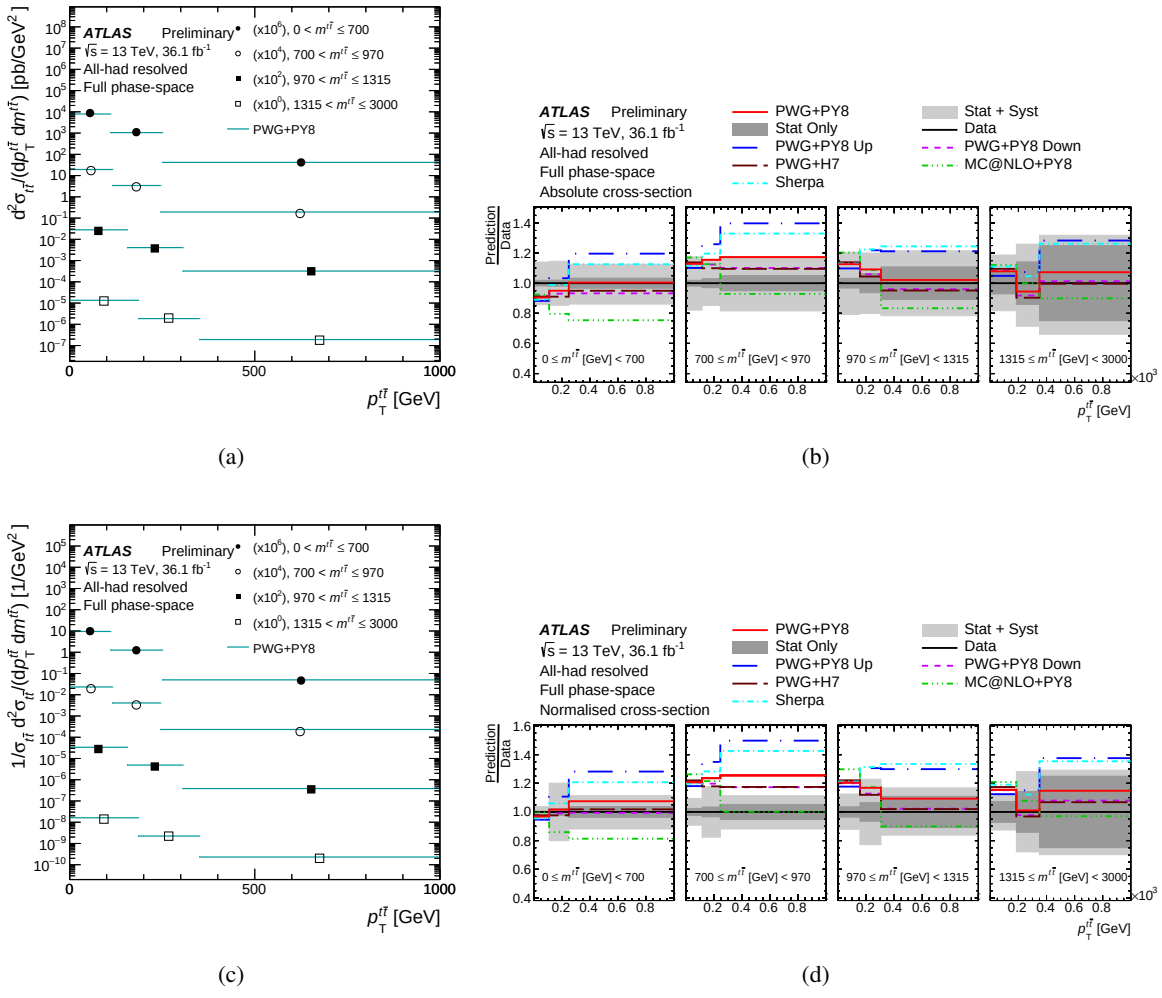

Figure 29: Absolute (a) and normalised (c) differential cross sections and absolute (b) and normalised (d) ratio of predictions over data in the full phase space as a function of $p_{\mathrm{T}}^{t\bar{t}}$ in bins of $m^{t\bar{t}}$. The shaded area represents the total statistical and systematic uncertainties.